UNIVERSITY OF CALIFORNIA SAN DIEGO

Silicon-Organic Slot Waveguide Directional Coupler for Photonic Switching and Sensing Applications

A dissertation submitted in partial satisfaction of the
requirements for the degree Doctor of Philosophy

in

Electrical Engineering (Photonics)

by

Li-Yuan Chiang

Committee in charge:

Paul K.L. Yu, Chair
Jinhye Bae
Shengqiang Cai
Yeshaiahu Fainman
Yu-Hwa Lo
Stephen A. Pappert

2022

The dissertation of Li-Yuan Chiang is approved, and it is acceptable in quality and form for publication on microfilm and electronically.

University of California San Diego

2022

DEDICATION

To my family

TABLE OF CONTENTS

LIST OF FIGURES

.

LIST OF TABLES

ACKNOWLEDGEMENTS

I would like to thank my advisors, Prof. Paul K.L. Yu and Dr. Steve Pappert, for their guidance and support. They have been helpful, careful, and supportive all the time during these years in my doctoral study. They provided research freedom and student-centered advising, making me enjoy doing research as they are. From technical insights, attitude, to manners, I have learned so much from them. I feel blessed and grateful to have them as my advisors along the journey.

I would like to acknowledge my committee members: Professor Jinhye Bae, Professor Shengqiang Cai, Professor Yeshaiahu Fainman, and Professor Yu-Hwa Lo, for their discussions and contributions to this dissertation.

I would like to thank Professor Chun-Ta Wang for providing fruitful discussions and inspiration in potential research directions. His cooperation and expertise in liquid crystal devices are valuable for me to finish this dissertation. I also thank for the help from my other co-coauthors and former lab members, Ting-Syuan Lin and Hao-Chi Liao.

To the friends I've made in San Diego, thanks for all the accompany, laughter, and remarkable memory we built together.

Finally, I appreciate my parents and wife for their support. They motivate me to pursue my dream and complete my life with happiness.

Chapter 2, in part, is a modified reprint of Li-Yuan Chiang, Chun-Ta Wang, Steve Pappert, and Paul K.L. Yu, "Efficient silicon photonic waveguide switches for chip-scale beam steering applications," *5th IEEE Electron Devices Technology & Manufacturing Conference*, (EDTM, 2021), WE2P2-3. The

dissertation author was the primary investigator and author of this material. I would like to acknowledge the Office of Naval Research (ONR) (contract N00014-18-I-2027) for the support of this work.

Chapter 3, in full, is a modified reprint of Li-Yuan Chiang, Chun-Ta Wang, Steve Pappert, and Paul K.L. Yu, "Ultralow-$V_{\pi}L$ Silicon Electro-Optic Directional Coupler Switch With a Liquid Crystal Cladding," *IEEE Photonics Technol. Lett.* **33**(15), 796-799 (2021) with additional details. The dissertation author was the primary investigator and author of this material. I would like to acknowledge the Office of Naval Research (ONR) (contract N00014-18-I-2027) for the support of this work.

Chapter 4, in full, is a modified reprint of Li-Yuan Chiang, Chun-Ta Wang, Ting-Syuan Lin, Steve Pappert, and Paul Yu, "Highly sensitive silicon photonic temperature sensor based on liquid crystal filled slot waveguide directional coupler," Opt. Express 28, 29345-29356 (2020) with additional details. The dissertation author was the primary investigator and author of this material. I would like to acknowledge the Office of Naval Research (ONR) (contract N00014-18-I-2027) for the support of this work.

Chapter 5, in part (Section 5.1-5.4), is a modified reprint of Li-Yuan Chiang, Hao-Chi Liao, Chun-Ta Wang, Steve Pappert, and Paul K.L. Yu, "Enhanced Thermo-Optic Efficiency of Silicon Photonic Switch with Passively Aligned Nematic Liquid Crystals," Photonics in Switching and Computing, (PSC, 2021), Tu3A.3 with additional details. The rest of Chapter 5 is currently being prepared for submission for publication of the material. Li-Yuan Chiang, Chun-Ta Wang,

Steve Pappert, and Paul K.L. Yu. The dissertation author was the primary investigator and author of these materials. I would like to acknowledge the Office of Naval Research (ONR) (contract N00014-18-I-2027) for the support of this work.

VITA

2015	B.S. in Engineering and System Science, National Tsing Hua University, Taiwan
2019	M.S. in Electrical Engineering (Photonics), University of California San Diego, USA
2022	Ph.D. in Electrical Engineering (Photonics), University of California San Diego, USA

PUBLICATIONS

Li-Yuan Chiang, Chun-Ta Wang, Ting-Syuan Lin, Steve Pappert, and Paul Yu, "Highly sensitive silicon photonic temperature sensor based on liquid crystal filled slot waveguide directional coupler," *Opt. Express* **28**, 29345-29356 (2020).

Li-Yuan Chiang, Chun-Ta Wang, Steve Pappert, and Paul K.L. Yu, "Efficient silicon photonic waveguide switches for chip-scale beam steering applications," *5th IEEE Electron Devices Technology & Manufacturing Conference*, (EDTM, 2021), WE2P2-3.

Li-Yuan Chiang, Chun-Ta Wang, Steve Pappert, and Paul K.L. Yu, "Ultralow-VπL Silicon Electro-Optic Directional Coupler Switch With a Liquid Crystal Cladding," *IEEE Photonics Technol. Lett.* **33**(15), 796-799 (2021).

Li-Yuan Chiang, Hao-Chi Liao, Chun-Ta Wang, Steve Pappert, and Paul K.L. Yu, "Enhanced Thermo-Optic Efficiency of Silicon Photonic Switch with Passively Aligned Nematic Liquid Crystals," *Photonics in Switching and Computing*, (PSC, 2021), Tu3A.3.

Li-Yuan Chiang, Chun-Ta Wang, Steve Pappert, and Paul K.L. Yu, "Power-efficient and compact silicon-organic thermo-optic switch based on a directional coupler," (in preparation)

FIELDS OF STUDY

Major Field: Electrical Engineering

Studies in Silicon Photonics
Professor Paul K.L. Yu and Doctor Stephen A. Pappert

ABSTRACT OF THE DISSERTATION

Silicon-Organic Slot Waveguide Directional Coupler for Photonic Switching and Sensing Applications

by

Li-Yuan Chiang

Doctor of Philosophy in Electrical Engineering (Photonics)

University of California San Diego, 2022

Professor Paul K.L. Yu, Chair

Silicon photonic waveguide devices are building blocks for designing photonic integrated circuits (PICs). Having high-performance device designs is vital to realize large-scale PICs for various emerging applications such as optical communications, light detection and ranging (LiDAR), and environmental/chemical/biological sensing. Directional coupler is one type of

essential component. This dissertation proposed a device platform based on slot waveguide directional couplers incorporated with nematic liquid crystals (NLCs). Combining the concentrated optical field confinement in the slot waveguide structure and the superior material properties of NLCs, the device platform showed efficient switching and sensing effects. We introduced two slot waveguide interferometers, directional couplers and Mach-Zehnder interferometers. The geometric dependence of the strip-loaded slot waveguide on tuning efficiency was systematically studied. By comparing the pros and cons of the two slot waveguide interferometers, we deduced that a directional coupler switch with high efficiency is more attractive in realizing a compact and low-loss switch design than an MZI switch. Three distinct devices were developed and demonstrated based on the Si-NLC directional coupler device platform with decent performance. Firstly, an EO switch showed ultralow $V_{\pi} \cdot L = 0.0195$ V·mm. The value corresponds to 19.5 μm of device length for the directional coupler switch operated with 1 V V_{π}. Secondly, a highly sensitive photonic temperature sensor reached a sensitivity as high as 1.6 nm/°C, benefiting from the large TO coefficient of NLC. The temperature sensitivity is one order of magnitude higher than other reported standard pure silicon photonic temperature sensors. Finally, a TO switch was demonstrated with a P_{π} as low as 0.58 mW. A technique was developed to passively align the NLC in the slot region of the device. The NLC provides a strong TO effect without the penalty of extra power consumption and electronic complexity to control the orientation of the molecules. The TO switch provides a new solution to make power-efficient TO actuators without sacrificing the response speed. In conclusion, the proposed Si-NLC device platform is a great candidate for high-performance device design, particularly for switching and sensing applications.

Chapter 1

Introduction

1.1 Silicon photonics

Silicon photonics is an advancing technology that has gained increasing attention in diverse applications, including optical communications [1], light detection and ranging (LiDAR) [2], quantum computing [3], artificial intelligence [4], and environmental/chemical/biological sensing [5]. The rapid technological advancement of silicon photonics benefits from the complementary metal-oxide-semiconductor (CMOS) fabrication techniques developed in the last several decades for electronic integrated circuits. Silicon photonics is based on a CMOS-compatible silicon-on-insulator (SOI) material platform comprised of silicon (Si) and silicon dioxide (SiO_2). An SOI wafer has a thin (commonly 220-330 nm) Si layer as the top layer, a μm-level SiO_2 layer as the buried oxide (BOX) in the middle, and a bulk Si layer as the substrate. The significant refractive index difference between Si and SiO_2 ($\Delta n \sim 2.0$) enables strong confinement of light in miniaturized Si structures. Si waveguides are one main kind of these miniaturized Si structures. Light can be confined and transported in a Si channel surrounded by SiO2 or partially air with proper design of the operating wavelength and waveguide geometry. As they are transparent in the infrared wavelengths, silicon waveguides are commonly designed for the 1.3 μm wavelength region at O-band or 1.55 μm wavelength region at C-band. A large variety of silicon photonic devices have been developed based on Si waveguides.

Silicon photonics is viewed as the photonic equivalent of silicon microelectronics in

many perspectives due to the overlapping fabrication and materials processing concepts. Silicon photonic devices are categorized into active devices and passive devices. Active devices generate, modulate, or detect light with an energy source for their operation, and their performance is related to the input signals. On the other hand, passive devices transmit and control light without an additional energy source. For specific applications, devices are connected by Si waveguides and densely integrated into photonic integrated circuits (PICs), similar to the case of an application-specific integrated circuit (ASIC) in electronics technology. In the same fashion, a photonic version of a field-programmable gate array (FPGA) called a programmable PIC was also developed with optical switches and mesh architectures [6].

A general metric for all kinds of silicon photonic chips and applications is optical insertion loss. Since light and the carried signals will be detected and identified after transmitting through complex and cascaded photonic structures on a PIC, a low on-chip loss is always desired. Lowering the optical loss of a device or structure provides it with the more substantial potential of scaling up and integrating with other components. The optical loss of a silicon waveguide is calculated from the output optical power divided by the input optical power. Losses in photonic waveguides stem from scattering, absorption, and radiation [7]. While designing photonic waveguides and devices, each loss factor needs to be considered.

Developing novel device structures, optimizing device geometry, and heterogeneous integration are three primary strategies to achieve better performance in silicon photonic devices. This dissertation covered all three directions during the device design stage. Through the process of design, modeling, fabrication, and measurement, several kinds of silicon photonic devices were demonstrated with decent performance. The devices developed are for switching and sensing applications.

1.2 Switching technology in silicon photonics

Electrically controlled photonic switches are used to redirect optical paths within PICs. The most common building blocks are 2x2 interferometric switches [8], with two input waveguides and two output waveguides in each switch. Light going into a 2x2 switch from one of the input channels can be arbitrarily controlled to come out from either one of the output channels. By cascading 2x2 switches in specific topologies, NxM switch fabrics can be constructed based on the requirements of applications [9]. Without being limited in power and data bandwidth as with electronic switches, silicon photonic switching is considered as a potential replacement for electronic switches in fiber-optic communications. This replacement also eliminates the inefficient and costly optical-electrical-optical (OEO) conversion required for electronic switches.

The optical phase tuning of individual 2x2 interferometric switches relies on either the electro-optic (EO) effect [10] or the thermo-optic (TO) effect [11]. Both effects result in material refractive index changes. They can be induced with externally applied electrical signals but in different mechanisms. For the EO effect, the refractive index of a material is in response to applied electric fields. It covers several distinct phenomena, such as the Pockels effect, Kerr effect, and reorientation of birefringent molecules. Alternatively, for the TO effect, refractive index changes are caused by temperature changes. This is usually implemented by an electrical current flowing through a resistive heater.

Efficiency and speed are two primary performance metrics for silicon photonic switches. With better efficiency, a photonic switch can be operated by lower driving voltage or minor power consumption. $V_\pi \cdot L$ product is a common quantity describing efficiency for EO switches, where V_π is the voltage required to complete one full on/off switching, and L is the length of the

active tuning region. An EO switch can always be designed longer for smaller V_π, but it comes with higher propagation loss and decreased modulation bandwidth in proportion to the increase of L. For TO switches, the efficiency is evaluated by P_π, the power consumption needed for one full on/off switching. The efficiency determines the feasibility of electrical driving, whereas the speed qualifies a switch for suitable applications. The speed of a switch must be fast enough to be practical for specific applications. The speed is evaluated with switching time t (10% to 90% for rising and 90% to 10% for falling) or switching time constant τ (0 to 63% for rising and 63% to 0 for falling) in this thesis, depending on the customs of the device category being discussed.

EO and TO switches have their respective advantages and challenges. EO switches support high-speed operations and applications with switching time on the nano-second level or faster. Still, the optical losses are high due to the free-carrier absorption (FCA) effect or rather long phase shifters. TO switches do not inherently induce optical loss from FCA. Their feature of lower loss is favorable for large-scale switch fabrics. However, a TO switch usually consumes a $P\pi$ of 10-30 mW to drive, where P_π is the power consumption required to complete one full on/off switching [9, 12]. The system's power budget and total power consumption of the switch fabrics limit the scaling of TO switches. In addition, the switching time of TO switches is usually on the micro-second level only.

1.3 Sensing in silicon photonics

Sensing via photonics is robust and immune to electromagnetic interference compared to electronic sensors. Photonic sensing is categorized into fiber-based and waveguide-based systems. Silicon photonics offers compact sensing functionality with silicon waveguides compared with fiber-based optical sensing. The strong confinement of light in silicon

waveguides provides significant light-matter interaction and the potential to make sensors with high sensitivities. The basic principle is to induce a refractive index change with a specific action in the silicon waveguide core or cladding material and detect the resulting optical responses. The degree of change from the particular activity is indirectly measured from the refractive index change. The idea can be realized in several ways for environmental/chemical/bio-sensing. Temperature sensing [13] is a significant direction for environmental sensor studies. Other examples include pressure sensing [14] and humidity sensing [15]. Contrastingly, chemical/bio-sensing is based on detecting and accumulating the responses of local refractive index changes [5, 16-17]. The refractive index changes come from different substances attached to the waveguides without selectivity. A widely used technique for chemical/bio-sensing to have selectivity in the sensed molecules is surface functionalization [18]. By coating the silicon waveguides with immobilized binder molecules, the waveguides can selectively capture the molecules of interest for sensing. Higher sensitivities are favorable for sensors, as the minimum detectable change in the refractive index is improved with a more sensitive sensor, providing a better detection limit. A popular way to improve the sensitivity is incorporating materials with large index changes in response to an external stimulus of interest. Liquid crystals are such materials. Liquid crystals possess attractive and stable material properties, making them a great candidate for silicon-organic hybrid devices.

1.4 Nematic liquid crystal (NLC)

Liquid crystal is a state of condensed matter with material properties between crystals and liquids. The molecules are rod-shaped. Macroscopically, the materials behave as a fluid, being able to flow at a significant rate. Microscopically, liquid crystal molecules have regional

orders and form domains. Within each domain, the molecules are aligned based on the same order. There are many liquid crystal phases with different molecule orders and different materials properties. The nematic phase is one of the most common liquid crystal phases. Although other liquid crystal phases may also be useful for silicon-organic photonic devices, they are beyond the scope of this dissertation.

In the nematic phase, organic liquid crystal molecules organize roughly parallel with their long molecular axes, appearing in directional order but in no positional order [19]. The nematic phase of liquid crystal materials and a single molecule are illustrated in **Figure 1.1**. Nematic liquid crystal (NLC) materials have several interesting favorable properties for silicon photonic

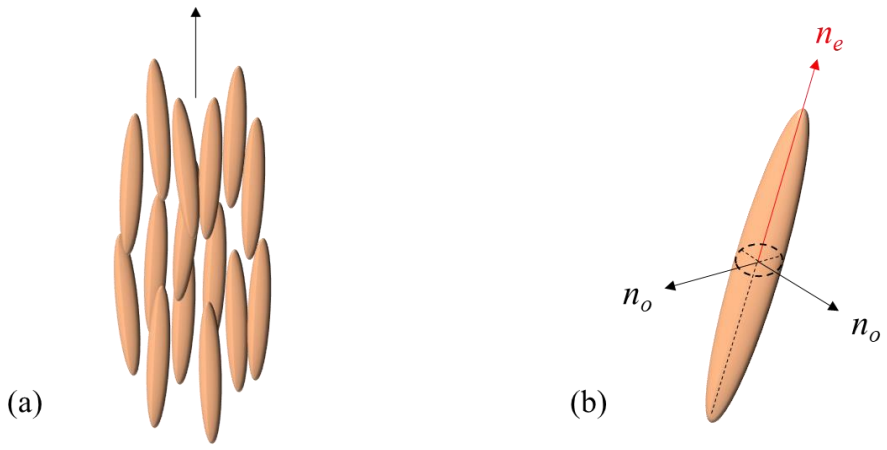

Figure 1.1: Illustrations of (a) the nematic phase of liquid crystals and (b) a single liquid crystal molecule with the corresponding optical birefringence

devices. Due to the rod-shaped molecules, NLC materials possess large birefringence Δn values on the order of 0.1-0.2. The NLC molecules are polar and have anisotropic dielectric properties. Therefore, the average direction of the long molecular axes can be controlled by an external electric field (**Figure 1.2**). The large birefringence and electrically controllable nature of NLC

provide a strong EO effect to be utilized in EO devices, such as liquid crystal displays (LCDs) [20]. Another attractive property of NLC materials is having a considerable TO effect along the long axes (dn_e/dT). This property makes NLC also an excellent material for TO devices.

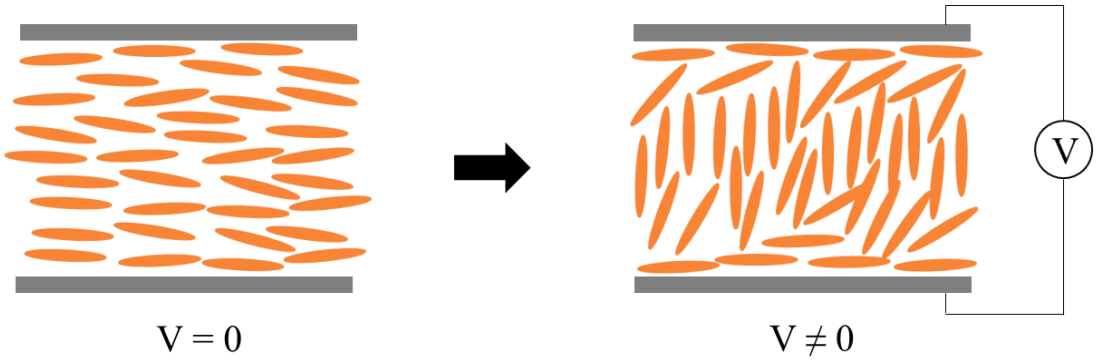

Figure 1.2: Illustrations of NLC reorientation induced by an externally applied electric field across two conductive panels

1.5 Dissertation overview

This dissertation explores Si-NLC integrated devices to realize performance enhancement for silicon photonic devices. Slot waveguide directional couplers are the device architecture employed to demonstrate an EO switch, a temperature sensor, and a TO switch.

In Chapter 2, slot waveguide interferometers are introduced. Two types of slot waveguide interferometers, Mach-Zehnder interferometers (MZIs) and directional couplers, are presented and compared. We deduced that a directional coupler switch with ultralow $V_\pi L$ is thus more attractive in realizing a compact and low-cost switch matrix design than an MZI switch. NLC-filled slot waveguide directional couplers are the device configuration used to demonstrate three kinds of silicon photonic devices. The device design, simulation, fabrication, and measurement results are included in the following chapters.

In Chapter 3, we propose a directional coupler EO switch with a record low of $V_\pi \cdot L$ = 0.0195 V·mm measured. The value corresponds to 19.5 μm of device length for the directional coupler switch operated with 1 V V_π. The results were compared with another reported Mach-Zehnder EO switch with the same silicon-NLC material system integrated into the slot waveguides. The fabrication process flow of our proposed device is illustrated in detail. The other devices in the following chapters also share similar fabrication process flows.

In Chapter 4, we focus on a highly sensitive photonic temperature sensor. Benefiting from the large TO coefficient of NLC, the Si-NLC hybrid sensor reached a sensitivity as high as 1.6 nm/°C, which is one order of magnitude higher than other reported pure silicon photonic temperature sensors. The slot waveguide directional coupler device configuration provides submicron one-dimensional spatial resolution and flexible selection in LC materials for designing temperature sensitivity and operational temperature range required by specific applications.

In Chapter 5, a TO switch is proposed and demonstrated with a P_π as low as 0.58 mW. Besides the design concept derived from the temperature sensor shown in Chapter 4, a technique was developed to passively align the NLC in the slot region of the device. In this way, the NLC provides a strong TO effect without the penalty of extra power consumption and electronic complexity to control the orientation of the molecules. By integrating NLC into the silicon TO switch, the low P_π was achieved without sacrificing the operation speed.

The dissertation is concluded in Chapter 6. The contributions and significance of the research topics are summarized. A discussion of future research directions in Si-NLC hybrid devices is provided.

Chapter 2

Slot waveguide interferometers

2.1 Slot waveguides

Proposed almost two decades ago, a silicon slot waveguide consists of two closely packed silicon waveguide arms horizontally separated with a narrow and fully etched slot [21]. The slot is filled with another material having a lower refractive index. The eigenmodes of the slot waveguide are formed by the interaction between the eigenmodes of the individual coupled arms. Due to the significant dielectric discontinuity at the high-index-contrast interfaces at the slot region, the optical field of the fundamental TE mode (TE0) is enhanced and confined in the slot. A schematic cross-section of the basic slot waveguide structure and the corresponding TE0 mode profile are shown in **Figure 2.1**.

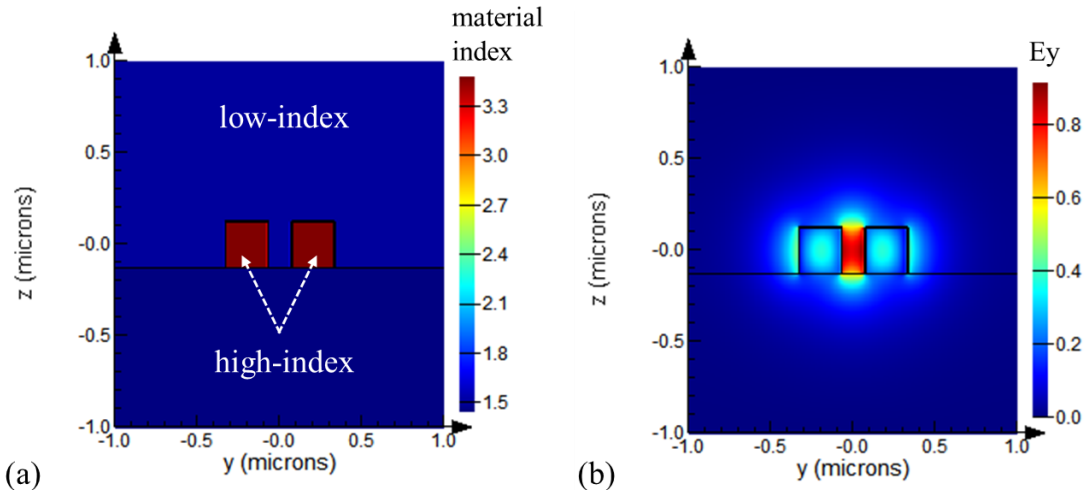

Figure 2.1: Cross-section schematics of (a) a slot waveguide and (b) the corresponding TE0 mode profile.

The strong optical confinement of the fundamental mode in the low-index slot provides better sensitivity to refractive index change in the slot region. The TE0 mode field is significantly more concentrated in a single area in slot waveguides compared to channel waveguides. In a channel waveguide, a larger portion of the field is concentrated in the waveguide core. The difference is shown in **Figure 2.2** with simulated mode distributions of the two waveguide structures. With the same material indices and silicon thickness, the geometries of the two waveguide examples were set to have the same simulated TE0 mode effective index n_{eff} = 1.936 as a benchmark. As the slot width or waveguide widths of the slot waveguide increase, the TE0 mode profile of the slot waveguide becomes more like that of two separate channel waveguides, due to the decreased mode confinement and field strength in the slot. Thus, the waveguide geometry design is critical for slot waveguides to realize their advantages.

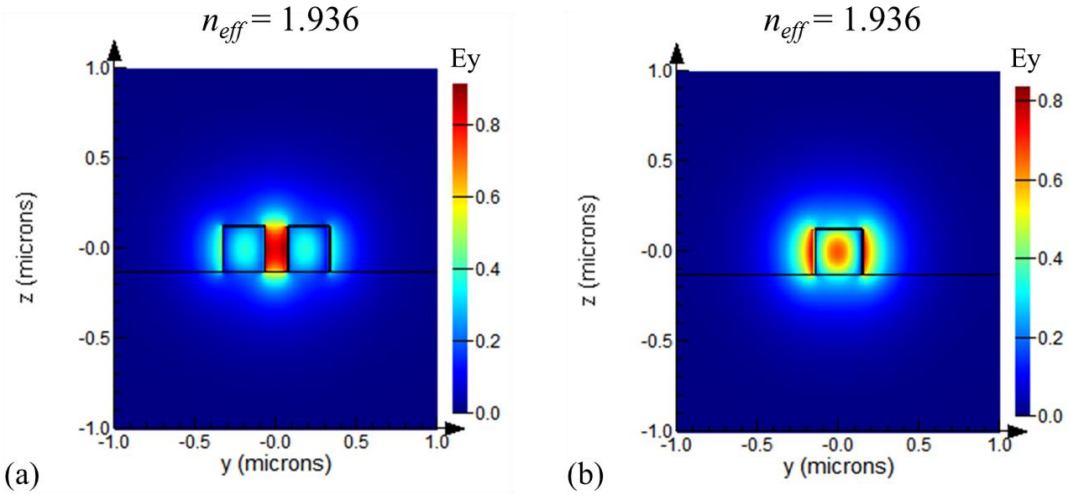

Figure 2.2: Simulated TE0 mode profiles of (a) a slot waveguide and (b) a channel waveguide.

In slot waveguides, the concentrated optical field outside of the silicon wires and higher

sensitivity to index change in the low-index slot are desirable properties for optical sensing [22] and switching [23]. Higher index change sensitivity means that a refractive index change Δn can induce a more considerable effective n_{eff} change. The slot region is thus the sensing hotspot in a slot waveguide. It is noteworthy that the concentrated optical field phenomenon in the conventional SOI slot waveguides only occurs in the TE0 mode instead of the TM0 mode. A simulated TM0 mode profile is shown in **Figure 2.3** with the same slot waveguide geometry as in **Figure 2.2(a)**. Since the electric fields and concentrated areas of the TM0 mode are in the vertical direction, there is no hotspot in the slot region.

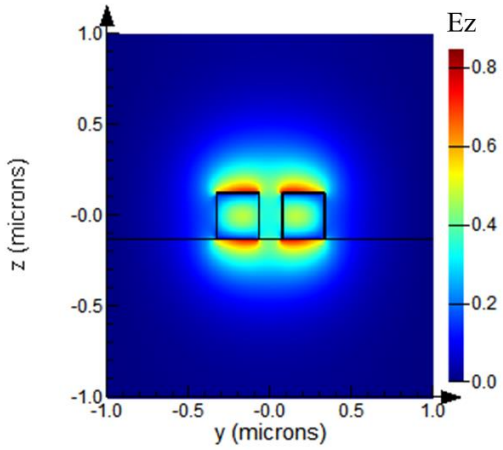

Figure 2.3: Simulated TM0 mode profiles of a slot waveguide.

Slot waveguides are commonly covered by certain cladding materials other than SiO_2. The cladding fills the nano-slot, and the material is chosen based on the target sensing/modulation applications. For chemical/bio-sensing, the cladding material is a solution containing the substance of interest to be detected [24]. For temperature sensing, the slot is filled with a temperature-sensitive material [25]. For switching and modulation, the cladding can be an

organic EO material enabling efficient refractive index tuning through an external electric field [26]. In the last case, a sample device structure based on the conventional SOI slot waveguides is shown in **Figure 2.4**. Two gold electrodes are placed away from the slot waveguide. A horizontal electric field can be applied through the slot waveguide. Since the sensing hotspot is in the slot, this configuration can be improved to be much more efficient if the electric field is applied only across the slot. It can be realized with a strip-loaded slot waveguide structure introduced in the next section.

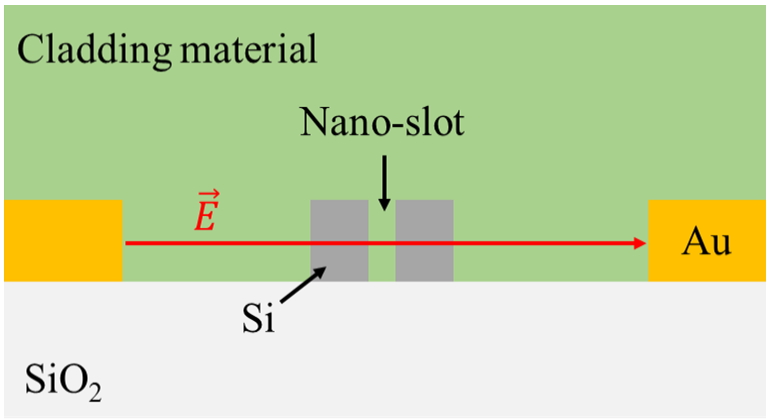

Figure 2.4: Cross-section schematic of an EO tunable device based on a conventional SOI slot waveguide and an electric field applied across the two gold electrodes.

2.2 Strip-loaded slot waveguides

The strip-loaded slot waveguide design was proposed to efficiently utilize the external electric field applied for EO tunable devices based on SOI slot waveguides [26-27]. As shown in **Figure 2.5**, a "strip-loading" region is a silicon thin slab connecting one slot waveguide arm and a metal electrode. The silicon slabs are formed by partially etching the silicon device layer in the SOI wafer. The silicon waveguide arms and slabs are doped to be conductive. With this

structure, the conductive boundaries of the two electrodes are extended to the inner sidewalls of the slot waveguide, and the external electric field drops across the narrow slot. Since metal electrodes are generally placed > 4 μm away from each other for optical loss consideration, and the slot width is usually made < 200 nm, the external electric field is more than one order of magnitude higher than the case depicted in **Figure 2.4** with the same voltage applied. Due to the advantage of the concentrated and highly overlapped optical field and electric field, the strip-loaded slot waveguide structure is a dominating design for slot waveguide EO devices. In a slot waveguide, a change of slot index Δn_{slot} induces an effective index change Δn_{eff} and a phase shift of the guided mode. The phase shift is typically linearly accumulated during the light propagation in the slot waveguide and thus proportional to the slot waveguide length. Such a device is called an EO phase shifter. To make a switch and be able to modulate light intensity, an interferometer structure is required.

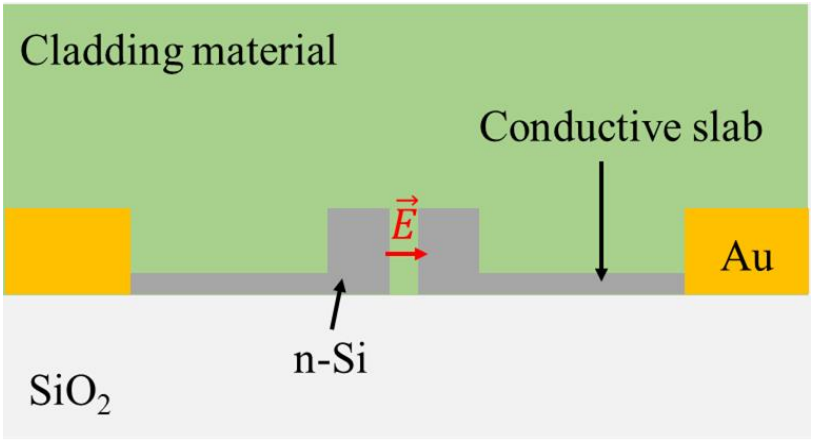

Figure 2.5: Cross-section schematic of an EO tunable device based on an SOI strip-loaded slot waveguide and two gold electrodes.

2.3 Slot waveguide Mach-Zehnder interferometers (MZIs)

A slot waveguide Mach-Zehnder interferometer (MZI) relies on interference from two arms of the slot waveguide [28]. The top view of a 2x2 EO switch based on slot waveguide MZI is depicted in **Figure 2.6**. Besides the two slot waveguide arms, the device consists of a pair of splitter/combiner, strip waveguides for routing, and strip-to-slot mode converters [29] the interfaces between the slot waveguides and strip waveguides. TE-polarized light enters the device from one of the input strip waveguides and is split equally into two strip waveguides. The light in both paths is converted from the strip mode to the slot mode. Light can be modulated in the region of slot waveguides with a device length L through the electrodes and conductive slabs. After passing through the slot waveguides, the slot mode is converted back to the strip mode. The light in both arms is merged into one of the output strip waveguides by a combiner and induces light interference. Assuming the two arms are symmetric without modulation, the resulting light has fully constructive interference in the bar output and fully destructive interference in the cross output. The switch is in the bar state in this condition. By modulating one of the two arms with an externally applied V_π, the resulting light can be changed to have fully constructive interference in the cross output. The switch is operated in the cross state in this condition. Intensity modulation is thus realized. The splitter/combiner is also called an optical 3-dB coupler. Directional couplers [30], adiabatic couplers [31], and multimode interference (MMI) couplers [32-33] are three main types of design for the splitters/combiners used in 2x2 MZI switches. Among the three types of 3-dB coupler, there exists a trade-off in device length and optical bandwidth. MMI couplers are the most widely used one due to the advantages of rather good fabrication tolerance and balancing in the trade-off between optical bandwidth and size. MZI switches with MMI couplers are less sensitive to wavelength and temperature change

during operation compared to switches based on resonant structures such as ring resonators [34-35].

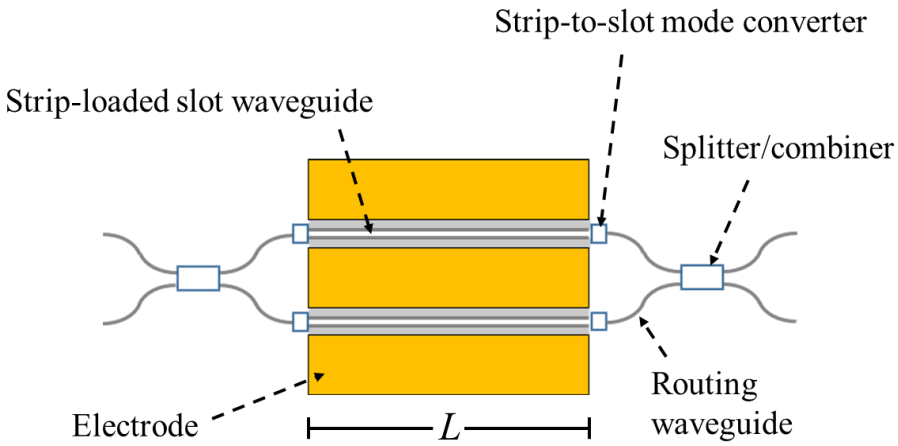

Figure 2.6: Top view of a 2x2 EO switch based on slot waveguide MZI.

2.4 Slot waveguide directional couplers

Slot waveguide directional couplers also rely on interference. Instead of only the fundamental mode, the interference in a directional coupler comes from the fundamental mode and first-order mode. The top view of a 2x2 EO switch based on a slot waveguide directional coupler is depicted in **Figure 2.7.** The device structure is simpler than the MZI case shown in **Figure 2.6**. In the directional coupler case, TE-polarized light in the fundamental mode enters one of the input strip waveguides. Propagating through an adiabatically transitional s-bend with an extended slab, the input light launches a linear combination of symmetric and anti-symmetric supermodes in the slot waveguide region [36]. The symmetric mode is the fundamental mode TE0, and the anti-symmetric mode is the first-order mode TE1. The mode profiles of the two modes are shown in **Figure 2.8**. Compared to the symmetric mode, the anti-symmetric mode has

a minimum field at the center of the slot region. Since the modulation depends on the overlap integral of an external electric field and the optical mode, the small net overlap of the anti-symmetric mode results in a small Δn_{eff} and phase shift when the slot index is modulated. The difference in the two-mode interference conditions leads to a switching behavior that can be measured from either one of the output strip waveguide ports. The initial interference condition without an external electric field is determined by several factors, different from the case of MZI.

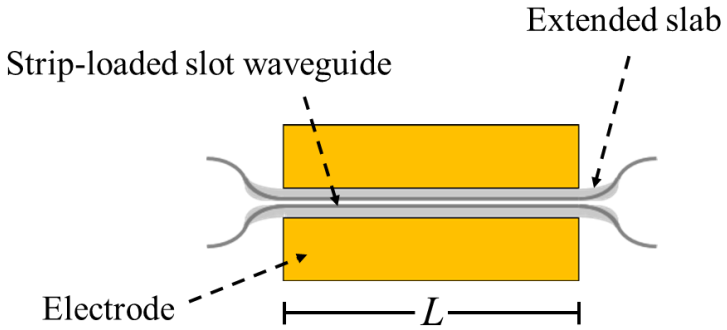

Figure 2.7: Top view of a 2x2 EO switch based on slot waveguide directional coupler.

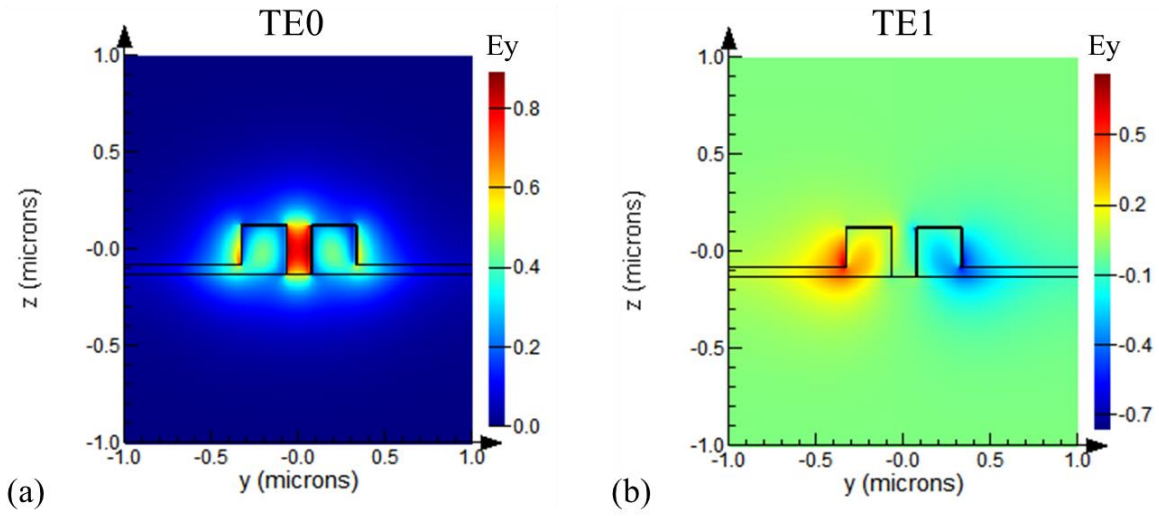

Figure 2.8: Simulated mode profiles of (a) the symmetric TE0 mode and (b) the anti-symmetric TE1 mode of a slot waveguide directional coupler.

2.5 Modeling and comparison of NLC-filled slot waveguide interferometers

The interference conditions and switching performance of the two slot waveguide interferometers introduced are quantitatively studied and compared in this section. It covers the principle, modeling, simulation results, and discussion in sequence.

2.5.1 Principle of operation

The two-mode interference of the two interferometers can be depicted as

$$L = m \cdot 2L_{cc} = \frac{m\lambda}{(n_{eff,1} - n_{eff,2})} \quad \textbf{(Equation 2.1)}$$

where L is the interactive length of the slot waveguide, m is the interference order (an integer for bar state or a half-order for cross state), L_{cc} is the cross-coupling length of the interferometer (the propagation length for the guided light to switch from one port to the other fully), λ is the wavelength in vacuum (λ = 1550 nm in the following modeling), and $n_{eff,i}$ (i = 1, 2) is the effective index of a specific optical mode. For the case of a directional coupler, $n_{eff,1}$ is for the symmetric mode TE0, and $n_{eff,2}$ is for the anti-symmetric mode TE1. For the case of an MZI, $n_{eff,1}$ is for the phase shifter arm, and $n_{eff,2}$ is for the reference arm. Since $n_{eff,1}$ theoretically equals $n_{eff,2}$ in a balanced MZI without voltage applied, an MZI switch initially has infinite L_{cc} and no cross coupling. On the other hand, the initial L_{cc} without voltage applied depends on the λ and waveguide geometry ($n_{eff,i}$) for a directional coupler switch.

2.5.2 Modeling and simulation results

The 2D finite element method (FEM) in Lumerical was used with the device cross

section (n_{Si} = 3.4803, n_{SiO2} = 1.444) shown in **Figure 2.9** to simulate the $n_{eff,i}$ results and study the geometrical dependence. E7, a commercially available nematic LC material with an ordinary refractive index n_o = 1.5022 and extraordinary refractive index n_e = 1.6961 at 25°C [37], is assumed in the simulations. Without an external electric field, the LC molecules in the slot region tend to align through the waveguide due to the physical confinement from the silicon sidewalls, and the slot index is n_o. With a sufficient electric field strength, the slot index is set to be n_e to represent the fully aligned LC parallel to the horizontal electric field. The two conditions were used in simulations to calculate the maximum number of π phase shifts ($\Delta\varphi$) at various waveguide geometries.

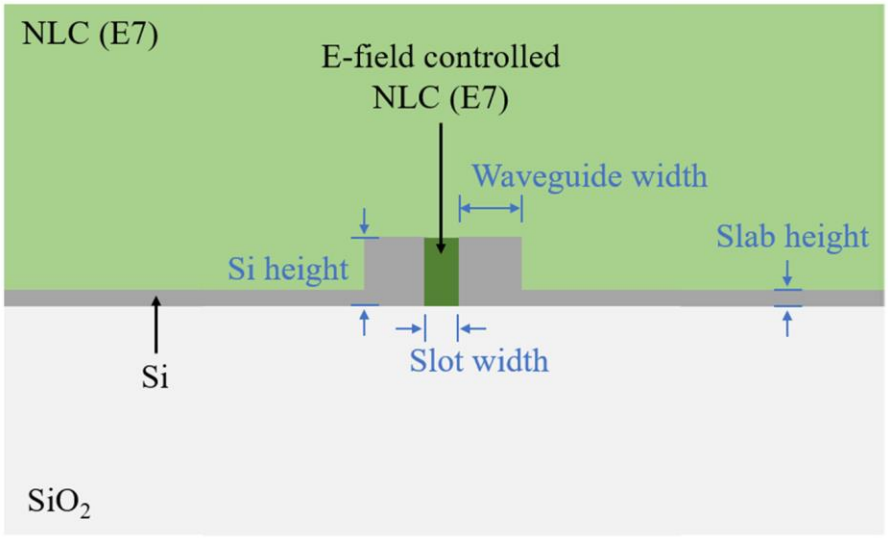

Figure 2.9: Device cross section used for Lumerical 2D FEM simulations. The materials are labeled in black color. The critical dimensions are labeled in blue color.

Assuming a fixed L = 1.5 mm, the systematic simulation results of $\Delta\varphi$ at each slot waveguide geometry were plotted in **Figure 2.10**, summarizing the $\Delta\varphi$ of a directional coupler switch and the relative difference of $\Delta\varphi$ between the directional coupler switch and an MZI

switch [38]. A higher $\Delta\varphi$ with the fixed L and slot width means that higher switching efficiency and lower $V_\pi L$ can be achieved with the device geometry. In **Figure 2.10(a)**, with a 250-nm device layer thickness and 140-nm slot width, the directional coupler switch is shown to be more efficient with thinner slabs. This originates from the condensing of the fundamental mode profile toward the center, creating a larger overlap in the slot region. With a 140-nm slot width and 50-nm slab height, it is shown in **Figure 2.10(b)** that increasing the silicon waveguide height from standard 220 nm to 330 nm leads to higher $\Delta\varphi$. This comes from the larger index-modulated slot region and mode overlaps between the electric field and optical fundamental mode. The results of 370 nm silicon waveguide height do not follow the trend due to the emergence of other undesired optical modes. As can be seen in **Figure 2.10(c)**, having a narrower slot width enhances the $\Delta\varphi$ of the device. Not only facilitating the optical mode confinement and fundamental mode overlap but a narrower slot width also means a stronger electric field across the slot with the same applied voltage. In experiments, however, the $V_\pi L$ may not always be lowered as the slot width is reduced. The sidewall anchoring effect of LC molecules acts as the counterforce of this trend [39-40]. There is thus an optimal slot width for the proposed switch, requiring further experimental studies to determine. For the waveguide width, the optimal value obtained from the simulation results is around 225 nm.

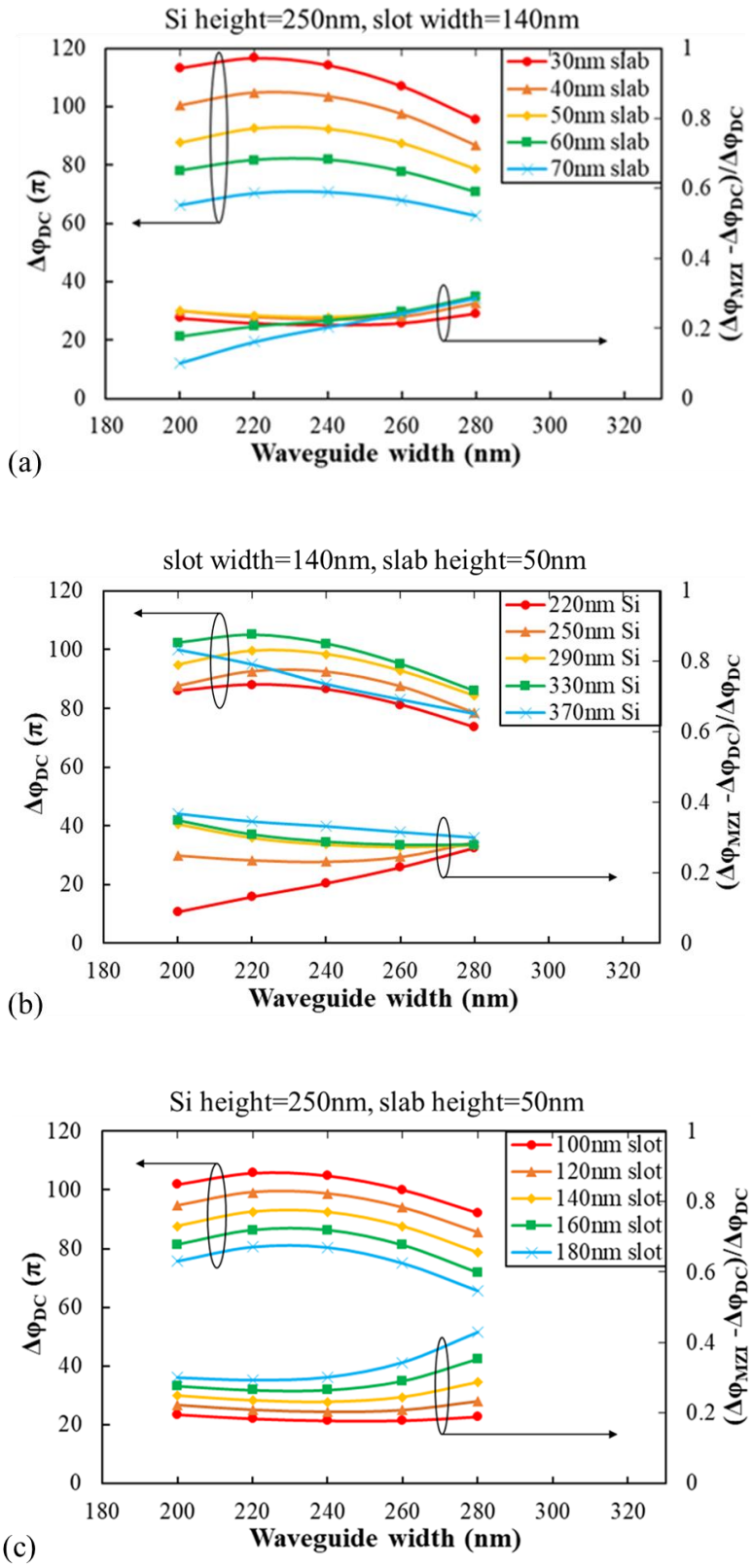

Figure 2.10: Device cross section used for Lumerical 2D FEM simulations.

2.5.3 Discussion

Although the $\Delta\varphi_{MZI}$ results are ~20% better than $\Delta\varphi_{DC}$ in an optimized structure, additional MMI couplers, routing strip waveguides, and strip-to-slot converters are required in the 2x2 MZI switch in both the input and output side compared to the directional coupler switch. Assuming a compact design, the additional MMI elements, routing strip waveguides, and strip-to-slot converters are estimated to occupy 30 μm, 5 μm, and 5 μm in length, respectively, ending up requiring an additional 80 μm in device length. For a design with $L < 400$ μm, the slot waveguide directional coupler switch starts to become more compelling compared to the MZI configuration. A 30π phase shift with a 1 V drive voltage and 1 mm long phase shifter has been demonstrated in an LC-filled MZI switch [40], implying that an LC switch with $L < 40$ μm can be realized. In addition to the device total length consideration, the directional switch is only about two-thirds the lateral size of the MZI switch resulting in a significant device surface area advantage. The proposed directional coupler switch with low $V_\pi L$ is thus attractive in realizing a compact and low-cost switch matrix design.

2.6 Conclusion

From the simulation results over a wide geometric design range, thinner slabs, thicker silicon waveguides, and narrower slot width generally lead to a more efficient electrically controlled LC-filled directional coupler optical switch and lower $V_\pi L$. Without the need for additional MMI couplers, routing strip waveguides, and strip-to-slot mode converters, the proposed directional coupler switch has strong potential to realize a more compact footprint and replace the MZI configuration for a switch design with an $L < 400$ μm.

2.7 Acknowledgement

Chapter 2, in part, is a modified reprint of Li-Yuan Chiang, Chun-Ta Wang, Steve Pappert, and Paul K.L. Yu, "Efficient silicon photonic waveguide switches for chip-scale beam steering applications," *5th IEEE Electron Devices Technology & Manufacturing Conference*, (EDTM, 2021), WE2P2-3. The dissertation author was the primary investigator and author of this material. I would like to acknowledge the Office of Naval Research (ONR) (contract N00014-18-I-2027) for the support of this work.

Chapter 3

An ultralow-$V_\pi L$ electro-optic (EO) switch

3.1 Introduction

Optical beam steering devices are key elements in light detection and ranging (LIDAR) technology. A solid-state optical phased array (OPA) [41-45] provides a high-speed, compact, lightweight, and cost-effective solution compared to the market-leading motorized optomechanical scanners [46]. For these reasons, the OPA is considered a strong candidate for future generations of beam steering devices for LIDAR applications. Although the OPA has become the dominant technology in the research of beam steering devices, switch-based beam steering [47-51] has several advantages over the OPA. It is also promising for future LIDAR products.

Silicon photonic switches [52] have recently shown great potential to form large-scale switch matrices for optical signal processing applications, including chip-scale LiDAR. First proposed in 2018 [47], a switch-based optical beam steering can be realized with an optical switch matrix, an emitter array, and a lens. A switch-based architecture has a power consumption that scales as $\log_2 N$, where N is the number of output ports. On the other hand, the power consumption of an OPA scales as N. The difference becomes larger for large-scale integration. For example, with $N = 1024$, the switch-based architecture only consumes ~1% of power compared to the OPA architecture. Besides power consumption, the switch-based architecture avoids the phasing operation of each phase shifter, and it allows multiple beams to be emitted

simultaneously. 2D beam steering on a single wavelength has been demonstrated with a switch-based architecture [49], providing a solution to overcome the challenge of limited wavelength tunability in OPAs and the cost of a tunable light source with a wide tuning range.

Within the mainstream silicon photonic switch technologies, which include electro-optic (EO), thermo-optic (TO), and microelectromechanical systems (MEMS), it is still challenging to demonstrate the sub-volt operation and power-efficient switching in a compact and low-loss device [52]. Silicon EO switches are the most suitable ones to be designed for sub-volt driving operation with low power consumption. However, they usually require an interactive length on the order of 1 cm or equivalent for just a single switch and lead to large footprints and high optical loss [53]. For the switch-based beamforming approaches, modulation efficiency ($V_\pi L$ product), footprint, and optical loss are the most critical criteria for optical switches due to the cascaded fabric and a large number of elements [9]. A miniaturized footprint enables a larger port count, reduced fabrication cost, and lower propagation loss. An ultralow-$V_\pi L$ photonic switch element can support sub-volt operation with short device length, facilitating compact, cost-effective, low-loss, and power-efficient switch matrices and optical beamformers.

Among various EO technologies on the silicon-on-insulator (SOI) platform, silicon-organic hybrid devices have made remarkable progress in achieving improved modulation efficiency (lower $V_\pi L$). Among the reported silicon-organic devices, EO polymers were utilized to demonstrate high-speed and efficient modulators for optical communication applications [54-57], whereas nematic liquid crystals (NLCs) provide even stronger but slower EO responses [58-60]. NLC-filled SOI slot waveguides have been the ones demonstrated with the lowest $V_\pi L$ results. By incorporating an NLC cladding with a silicon conductive slot waveguide Mach-Zehnder interferometer (MZI), a $V_\pi L$ as low as 0.0224 V·mm was demonstrated [40]. For LIDAR

beam steering applications, switching speed is not a major consideration, making NLC technology very competitive.

Plasmonic-organic hybrid (POH) devices are another way to realize ultralow $V_\pi L$. Combining plasmonic slot waveguides with highly efficient EO polymers, a $V_\pi L$ of 0.05 V·mm was demonstrated [61]. However, the high optical loss of the POH structures results in loss-efficiency products ($aV_\pi L$, where a is the optical propagation loss of the device region in dB/mm) larger than 20 V·dB [61]. In comparison, the NLC-cladded silicon slot waveguide MZI switch was demonstrated with an $aV_\pi L$ of ~0.25 V·dB [40].

Most NLC optical switches demonstrated to date employ an MZI device configuration [40, 58, 62]. In this chapter, we propose and demonstrate a silicon photonic EO switch based on an NLC-cladded slot waveguide directional coupler [63]. We show a $V_\pi L$ of 0.0195 V·mm at an operating point of 0.935 V root-mean-square voltage for wavelengths near 1550 nm. To the best of our knowledge, the $V_\pi L$ value is the lowest reported to date. This device offers the potential of sub-volt V_π switching operation with a device length as short as 20 μm. The device design, fabrication process flow, and experimental results are shown in the following sections. We then compare the directional coupler switch with the MZI switch in a table and display the directional coupler's competitiveness for designing compact and low-loss switch elements.

3.2 Device design

Figure 3.1 shows the proposed silicon photonic switch based on a slot waveguide directional coupler with an NLC cladding filling the slot region [63]. A strip-loaded conductive silicon slot waveguide structure enables a highly confined external electric field across the slot [26], allowing efficient refractive index tuning of the NLC in the slot region through reorienting

the rod-shape molecules. The NLC material employed in this work is E7 (made by Merck), which has a large birefringence (Δn~0.2) contributing to the strong EO response.

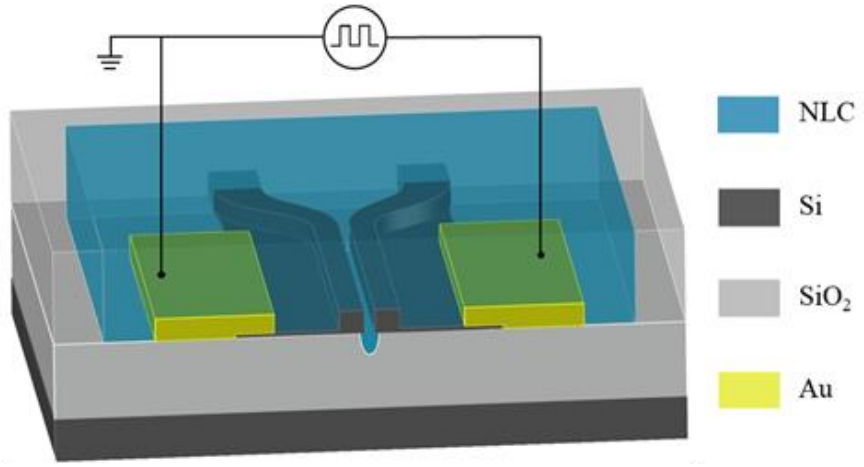

Figure 3.1: Schematic of the proposed silicon EO switch. The slot waveguide directional coupler is cladded with a nematic liquid crystal (NLC) layer.

Two optical modes, TE0 and TE1, propagating in the slot waveguide directional coupler are launched by a single-mode TE-polarized light at a wavelength near 1550 nm from either one of the input waveguides. The TE0 and TE1 mode profiles, as shown in **Figure 3.2,** have distinct mode overlaps at the slot region, leading to the contrasting effective index changes while tuning the slot material index. Optical switching is achieved by tuning the two-mode interference condition,

$$L_{cc} = \frac{\lambda}{(n_{eff,0} - n_{eff,1})} \qquad \textbf{(Equation 3.1)}$$

where λ is the light wavelength, L_{cc} is the cross-coupling length, $n_{eff,0}$ and $n_{eff,1}$ are the electric-field dependent effective indices of the TE0 and TE1 modes, respectively. The waveguide geometry-dependent switching performance is systematically studied using 2D Finite Difference Eigenmode (FDE) simulation. The results are summarily reported in Chapter 2 and in [38]. The

targeting waveguide geometry for device fabrication was selected based on the FDE simulation results on efficiency.

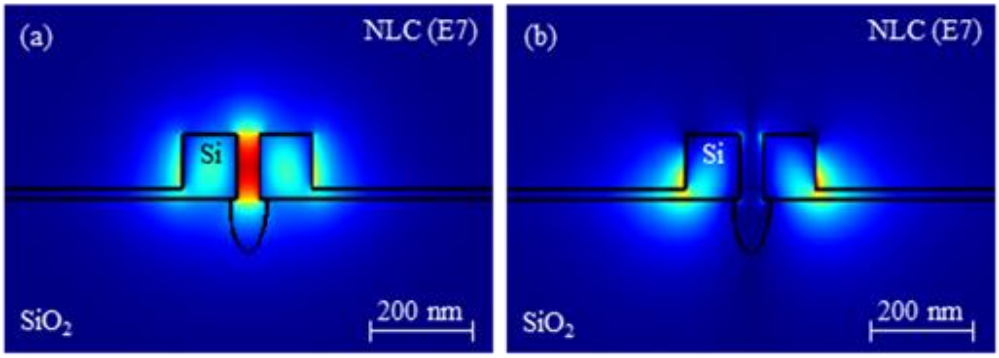

Figure 3.2: Optical mode profiles of the (a) TE0 mode and (b) TE1 mode propagating in the cross-coupling slot waveguide of the proposed EO switch.

3.3 Device fabrication

The photonic switch was fabricated using a silicon-on-insulator (SOI) wafer with a 250 nm silicon layer on top of a 3-μm buried oxide layer. The detailed fabrication process flow is illustrated step-by-step in **Figure 3.3**. The device cross section of each stage during the processing was shown. The label above the black arrows between cross section figures depicts the corresponding fabrication processes. In the beginning, the silicon strip-loaded slot waveguide structure was patterned using electron-beam lithography (EBL) and formed using reactive ion etching (RIE) with SF_6:CHF_3 plasma. The electron-beam resist for the etching mask is hydrogen silsesquioxane (HSQ), which operates as a negative resist and turns into low-density SiO_2 through electron-beam exposure. The slot waveguide has a 1.5 mm long and 115 nm wide slot region. The waveguide width is 265 nm for both silicon-coupled arms. The silicon slabs have a thickness of 45 nm. After forming the strip-loaded slot waveguide, the HSQ was removed via

diluted buffered oxide etch (BOE), as shown in **Figure 3.3(d)**. A 100 nm thin layer of SiO_2, as a protection layer, was deposited on the sample by plasma-enhanced chemical vapor deposition (PECVD). The silicon coupled arms and slabs were n-doped at $10^{17}/cm^3$ so that they are conducive. The silicon slabs were n-doped again at $10^{20}/cm^3$ to form Ohmic contact with metal electrodes later. A 6 µm photoresist mask was used as the ion implantation mask. A photoresist implantation mask needs to be thick enough for the corresponding implant energy and dose, otherwise, it will be hard to remove after doping. After removing the implantation masks completely, dopant activation was performed with rapid thermal annealing (RTA) at 1050°C for 1 minute. The waveguide structures are cladded with a 2 µm SiO_2 layer by PECVD, as shown in **Figure 3.3(l)**. The slot region was opened and overetched through a combination of RIE and BOE. The BOE helps cleaning up the sidewall's SiO_2 residues effectively after RIE. Cr/Au contacts were formed by sputtering and lift-off processes. E7 NLC was deposited on the chip as the final step to fill the slot and overetched region, utilizing its fluidic nature. The finished device cross section is shown in **Figure. 3.3(t)**.

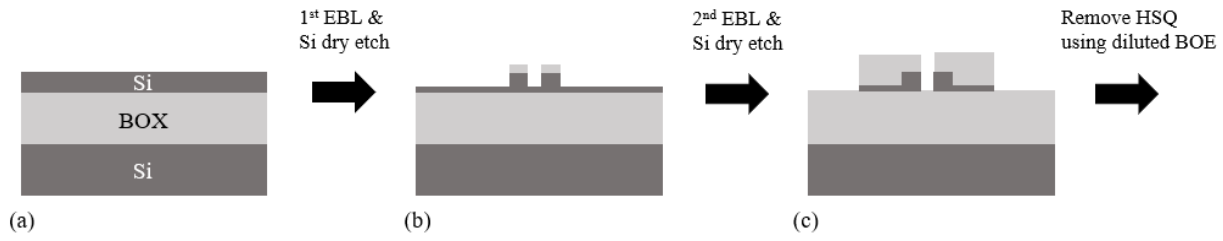

Figure 3.3: Schematic representation of the fabrication process flow of the proposed EO switch. The device cross sections during the processing are illustrated step by step.

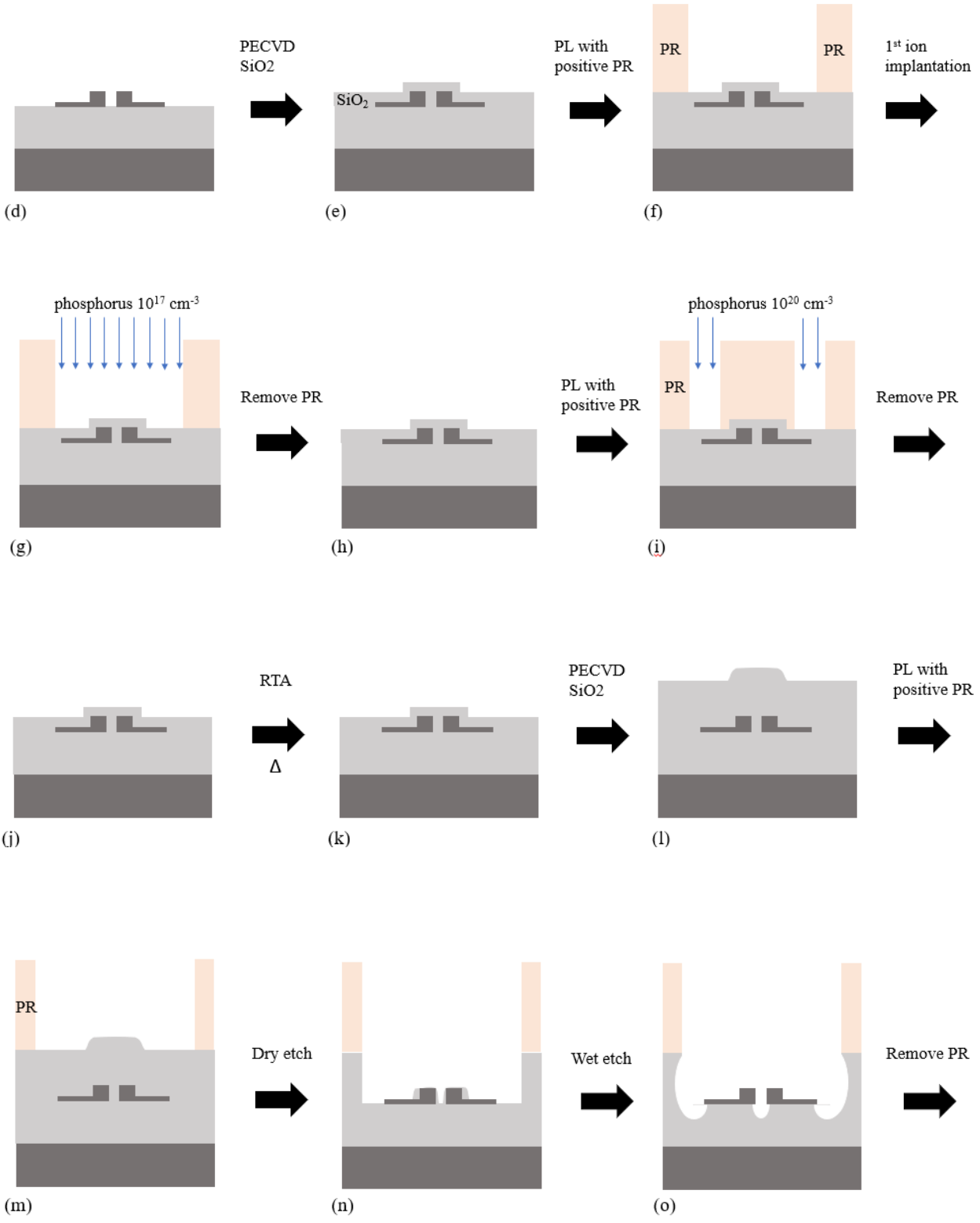

Figure 3.3: Schematic representation of the fabrication process flow of the proposed EO switch. The device cross sections during the processing are illustrated step by step. (Continued)

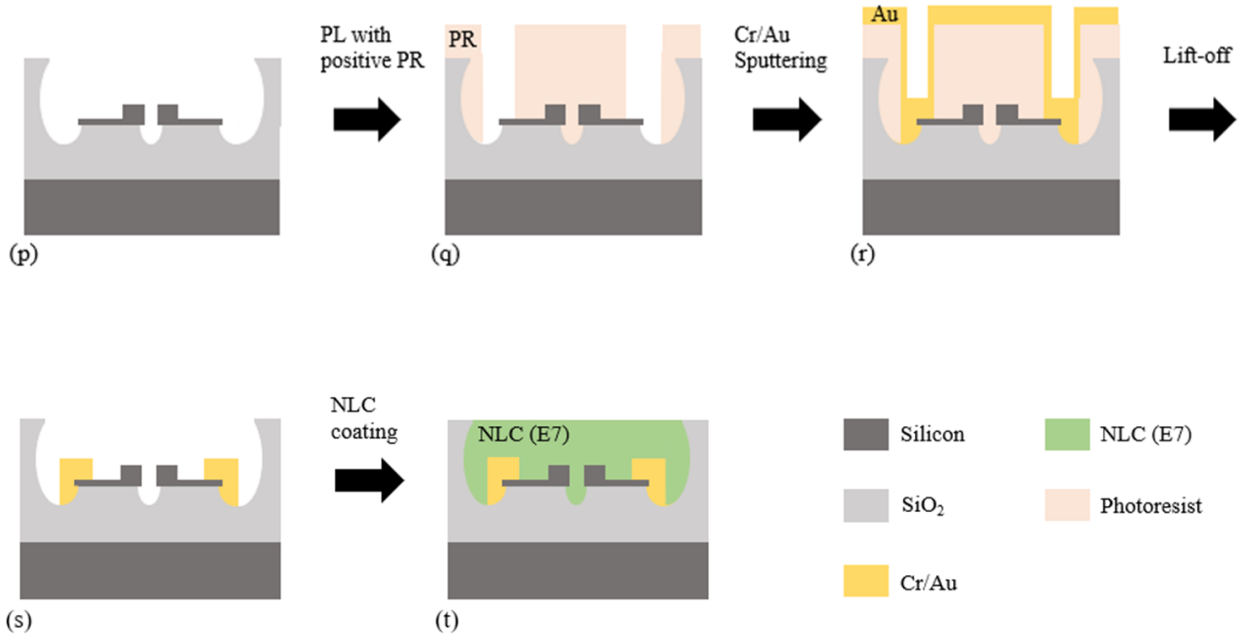

Figure 3.3: Schematic representation of the fabrication process flow of the proposed EO switch. The device cross sections during the processing are illustrated step by step. (Continued)

Figure 3.4(a) and **Figure 3.4(b)** show the top view and slot cross section of the structure, respectively, before applying the NLC. The images were taken under a scanning electron microscope (SEM). The slot region was intentionally overetched during fabrication. The overetch ensures the slot was cleared from the remaining PECVD SiO_2 and ready for NLC filling. Also, since the solid boundaries anchor a portion of NLC molecules and make them hard to be reoriented [64], keeping the bottom SiO_2 boundary away from the bottom of the slot allows better control of the NLC molecules throughout the silicon slot.

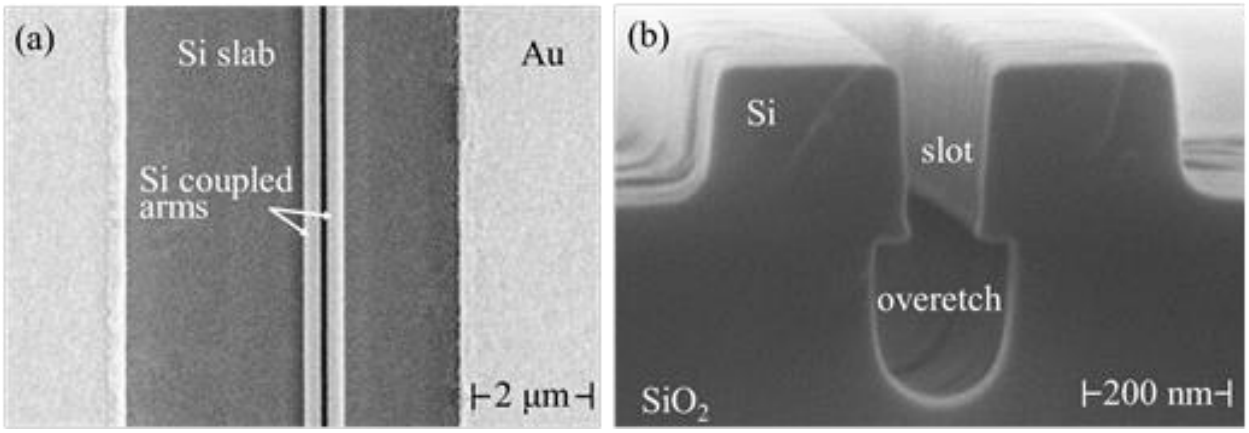

Figure 3.4: SEM images of the proposed device displaying (a) top view and (b) expanded cross section view before applying an NLC cladding.

3.4 Device Characterization

The photonic switch was driven with 5 kHz square-wave alternating current (AC) voltage to avoid degradation of the NLC material in the slot region [65]. The molecular directions of the NLC in the slot were tuned by changing the amplitude of the square-wave signal to achieve optical switching. The optical transmission and switching results as a function of the applied root-mean-square voltage measured from one of the output ports are shown in **Figure 3.5**. Operating at 0.935 V, a V_π of 0.013 V was measured as shown in **Figure 3.5(a)**. The corresponding $V_\pi L$ is 0.0195 V·mm. The device was switched on and off 10 cycles with the 0.928 V and 0.941 V applied as shown in **Figure 3.5(b)**. The device was also measured with 100 switching cycles. The standard deviation values calculated from the 100 on-state and off-state signal levels are 0.17 dB and 0.11 dB, respectively. The average extinction ratio measured is ~9 dB over the cycles.

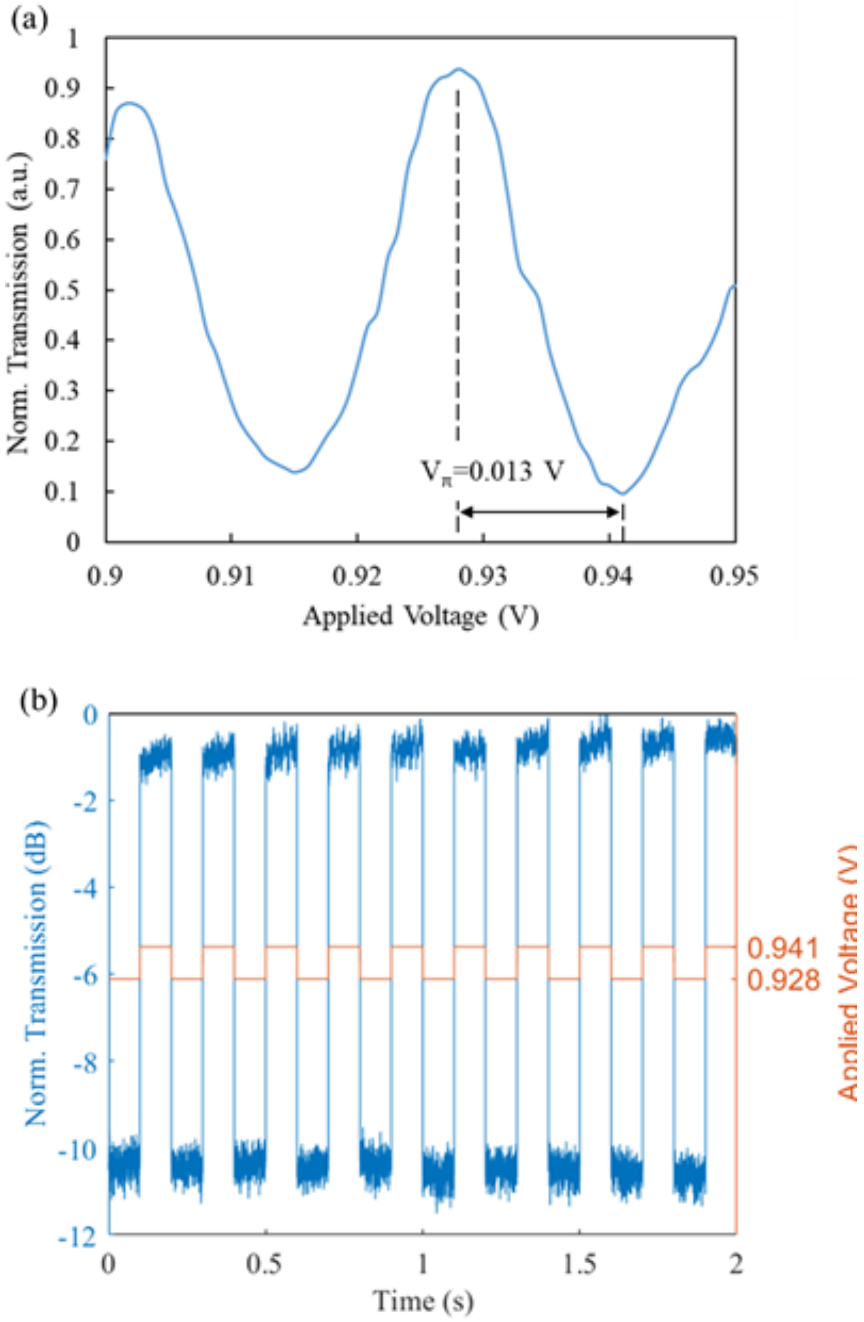

Figure 3.5: (a) Normalized optical transmission of the device as a function of the applied voltage (b) Real-time trace of the device's optical transmission during 10 switching on and off cycles shown with the corresponding applied voltage.

The temporal response of on/off switching between 0.928 V and 0.941 V measured from the device optically and the probe tips electrically, respectively, are shown in **Figure 3.6**. The

measured 10%-90% rise time is 1.41 ms, and the 90%-10% fall time is 1.37 ms for the device, both limited by the electrical driving. The on-chip loss of the directional coupler switch is -4.8 ± 0.8 dB. The $aV_{\pi}L$ calculated is therefore 0.0624 V·dB. We expect a better extinction ratio and optical loss can be achieved with optimization of fabrication processes and coupling between the input/output waveguides and the slot waveguide.

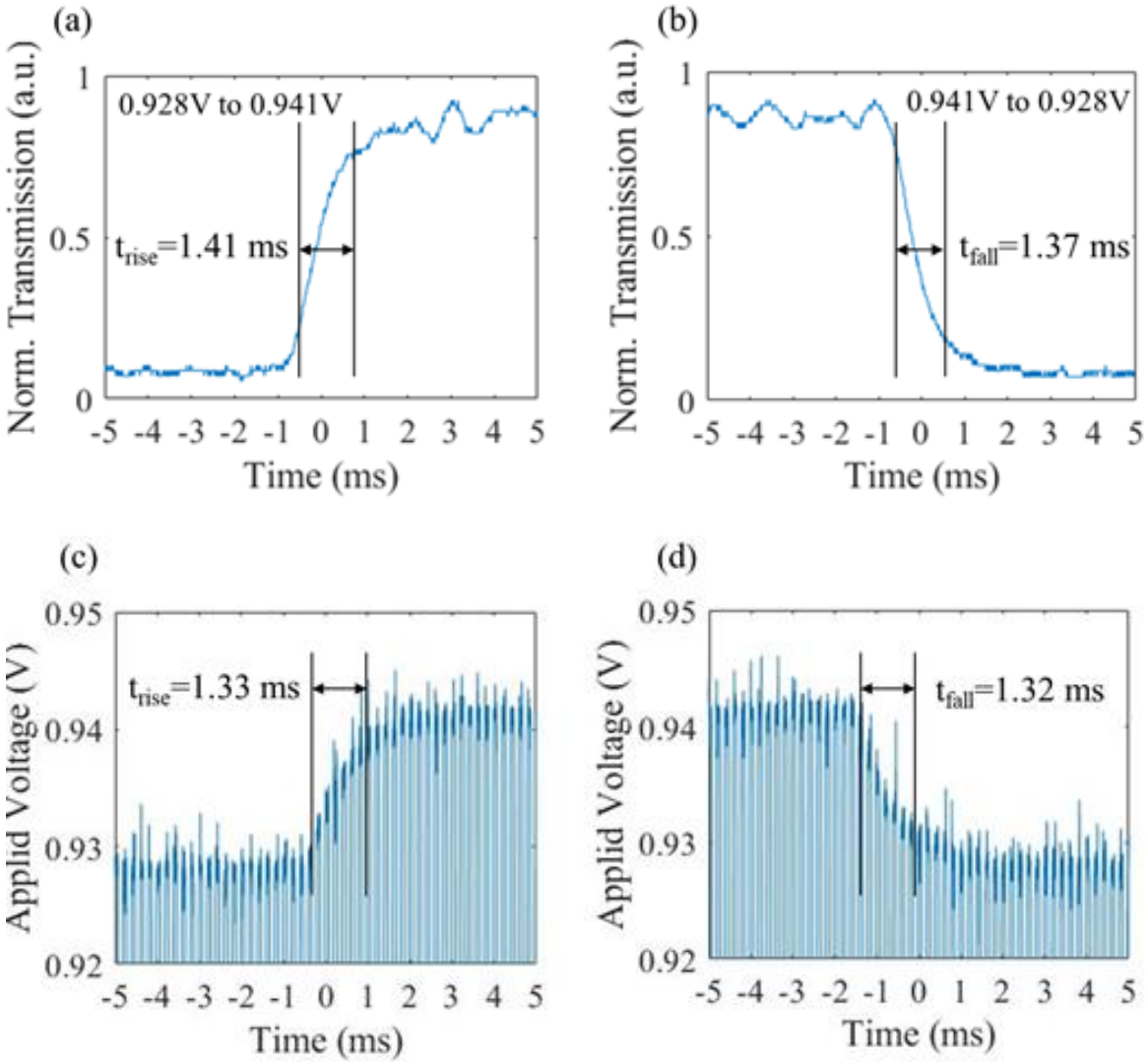

Figure 3.6: Measured temporal responses of optical (a) switching on and (b) switching off from the device. Electrical driving of (c) switching on and (d) switching off measured from the probe tips.

3.5 Discussion

This section starts with a comparison between the proposed directional coupler switch with a reported MZI switch to show the superior performance of our proposed device. Both devices are NLC-filled slot waveguide EO switches. Then, we discuss the device length effect and operation frequency based on the measurement results. Finally, the advantageous NLC material properties and the potential directions of NLC materials improvement are covered.

3.5.1 Comparison of the directional coupler switch and the MZI switch

In addition to a directional coupler format having TE0 and TE1 mode interference, the slot waveguide configuration can also be incorporated into an MZI having interference of two TE0 modes in separate slot waveguides. The demonstrated performance of our directional coupler switch was compared to that of a reported slot waveguide MZI switch [40] and is listed in **Table 3.1**. Using the same NLC material E7, the directional coupler switch achieved smaller $V_{\pi}L$ and on-chip loss than the MZI switch. Regarding the operating point and switching time of the directional coupler and MZI devices, since they are both limited by the NLC material properties, there is no significant difference.

Table 3.1: Comparison of demonstrated NLC-filled slot waveguide switches.

Device Architecture	Slot WG directional coupler switch (This work, [63])	Slot WG MZI switch [40]
NLC material	E7	E7
$V_\pi L$ (V·mm)	0.0195	0.0224
Operating Point (V)	0.935	~1.0
V_π (V)	0.013	0.0224
L (mm)	1.5	1
On-chip loss (dB)	-4.8	-11.0
$\alpha V_\pi L$ (V·dB)	0.0624	0.2464
Switching time (ms)	< 1.5	< 2

The improved efficiency of the directional coupler switch originates from the optimization of slot waveguide geometry, instead of the physical nature of the device architecture. The modulation efficiency is highly dependent on both the slot waveguide geometry and NLC material properties. From our previous simulation results [38], increased silicon waveguide height (up to 330 nm), narrower slot width, and lower slab height provide larger mode overlap of the TE0 mode in the slot region. With larger mode overlap confined in the slot region, the effective index of the TE0 mode is more sensitive to slot index tuning. The effects of material properties on device performance are more complex. Using the same NLC material, variations of the anchoring strength, sidewall roughness, and slot geometry can affect the EO modulation efficiency [66-67].

In principle, with the same slot waveguide geometry and NLC material properties, an MZI switch has a higher efficiency compared with that of a directional coupler switch [38]. This is due to the unwanted and inevitable modulation of the TE1 mode in the directional coupler switches. Despite having a higher efficiency, the MZI is not always the better option to configure

photonic switches. Combiner/splitter, additional routing waveguides, and strip-to-slot mode converters are required at both the input and output sides of an MZI switch, contributing to excess optical loss and large device footprint. These elements are not scalable with improved efficiency and shorter slot waveguide length. For ultra-compact switch design, the directional coupler can be preferable due to its potentially smaller footprint and lower optical loss. For example, based on simulations and the demonstrated $V_\pi L$ of 0.0195 V·mm from the directional coupler switch, we project a $V_\pi L$ of 0.0142 V·mm can be achieved if the device is patterned as an MZI switch. The values correspond to 19.5 μm and 14.2 μm of device lengths for the directional coupler and MZI, respectively, operated with 1 V V_π. However, this is not the enitre story. Whereas 5.3 μm shorter in the estimated slot waveguide region, typical MZI switches require a pair of ~30 μm long multi-mode interferometers (MMIs) [68], ~5 μm long additional routing waveguides, and ~5 μm long strip-to-slot converters [69], making it extremely challenging to design an MZI switch with a total length in the tens of micrometers. Therefore, for switches requiring a small footprint, the advantage of better efficiency in an MZI device is no longer the dominant design consideration.

Along with a smaller longitudinal size for ultra-compact device design, the directional coupler architecture is also smaller in lateral footprint. Assuming 5 μm of metal contact width and 4 μm of separation between metal contacts, the lateral sizes of the ultra-compact directional coupler and MZI switch will be 14 μm and 18 μm, respectively. With the demonstrated $V_\pi L$ and device lengths assumed in the previous paragraph, the directional coupler configuration only occupies < 20% of the device area compared with the MZI configuration. The small footprint and low loss characteristics make the directional coupler architecture a leading candidate for ultralow-$V_\pi L$ photonic switch elements in cascaded switch arrays.

3.5.2 Device length effect

It is worth noting that the demonstrated device with 1.5 mm device length is highly wavelength dependent due to the small free spectral range (FSR) of ~4.5 nm. And the -4.8 dB loss is too high for cascaded switch arrays. However, the FSR is inversely proportional to the device length, and the propagation loss is proportional to the device length. The projected device with only 20-μm length is expected to possess a broadband FSR of ~337.5 nm and low-loss characteristics favorable for switch array applications.

3.5.3 Operation frequency and power consumption

Since the device is operated with 5 kHz square-wave AC voltages, the static power consumption to maintain optical signal level 0 and level 1, P_i (i = 0, 1), can be calculated from

$$P_i = f \cdot C \cdot V_i^2 \qquad \textbf{(Equation 3.2)}$$

where f is the frequency of the AC voltage, C is the capacitance of the slot capacitor, and V_i is the corresponding voltage at the signal level (i = 0, 1). The measured C at 5 kHz and 1 V is approximately 130 fF. Using V_i = 1V, we can estimate the upper limit of the total power consumption, including static and switching, to be 0.6 nW.

It is indicated in the power consumption analysis that a lower driving frequency is preferred to operate the device with a higher power efficiency. Another consideration of the operation frequency is to maintain a fairly high frequency for stable optical signal levels. If the applied frequency is comparable to the NLC response speed, the NLC molecules will keep reorienting with the applied AC voltage and the optical signal levels will be unstable. In other words, there is a trade-off between the device speed and power consumption.

3.5.4 NLC materials

In this work, we chose the widely used E7 as the NLC cladding to demonstrate the device. However, it is worth noting that the NLC material can be flexibly chosen based on different design considerations such as efficiency, switching speed, and power consumption. In general, NLC materials with high birefringence and low viscosity are preferred due to the resulting stronger and faster EO responses [70]. The dielectric anisotropy, elastic constants, and anchoring strength of NLC materials are also critical properties to achieve further improved efficiency and lower operation voltage [40, 58, 71].

Incorporating additives into NLC materials is another strategy to improve NLC material properties for EO applications. To incorporate NLC with additives into the proposed device, the additive unit size and slot width need to be considered. For instance, C_{60} [72], gold nanoparticles [73], and cadmium selenide quantum dots (CdSe QDs) [74] were reported to be dopants to successfully improve the NLC EO performance. Although more studies are required to know if these materials will provide the claimed improvement for application within a silicon nano-slot, these methods are encouraging for further enhancement of the performance of the directional coupler switch.

3.6 Conclusion

We have experimentally demonstrated a silicon photonic directional coupler switch with 0.0195 V·mm modulation efficiency and 0.0624 V·dB loss-efficiency product. We have compared this directional coupler switch performance with similar MZI switch device architectures. Without requiring a pair of combiner/splitter, additional routing waveguides, and strip-to-slot converters, we find the directional coupler switch is superior to a corresponding MZI

switch for efficient, compact optical switching due to a comparably smaller device footprint and lower optical loss. Improved directional coupler performance can be expected as improved NLCs are incorporated into the switching devices.

3.7 Acknowledgement

Chapter 3, in full, is a modified reprint of Li-Yuan Chiang, Chun-Ta Wang, Steve Pappert, and Paul K.L. Yu, "Ultralow-$V_{\pi}L$ Silicon Electro-Optic Directional Coupler Switch With a Liquid Crystal Cladding," *IEEE Photonics Technol. Lett.* **33**(15), 796-799 (2021) with additional details. The dissertation author was the primary investigator and author of this material. I would like to acknowledge the Office of Naval Research (ONR) (contract N00014-18-I-2027) for the support of this work.

Chapter 4

A highly sensitive photonic temperature sensor

4.1 Introduction

Besides EO devices, TO devices were also investigated as the other main direction of this dissertation utilizing the desirable TO properties of NLC materials. Optically based temperature sensors have attracted growing interest recently due to advantages such as compact size and immunity to electromagnetic interference [75-76]. Compared to fiber-optic [77-81] and other waveguide-based [82-85] temperature sensors, silicon waveguide temperature sensing devices based on the SOI platform benefit from mature CMOS fabrication techniques and ease of integration with other devices for on-chip applications. A highly sensitive optical temperature sensor based on two-mode interference modulation within a silicon slot waveguide structure is theoretically proposed and experimentally demonstrated in this chapter.

Silicon waveguide temperature sensors have been demonstrated with various device configurations, including MZI [86-88], MMI [89], micro-ring resonator [13, 90-91], waveguide Bragg gratings (WBGs) [92], two-dimensional (2D) photonic crystal waveguide [93], and photonic crystal nanobeam cavities [94]. However, their temperature sensitivities, defined as wavelength shift over a temperature change, are limited due to the strong optical confinement of silicon waveguides in the SOI platform and the intrinsic thermo-optic coefficient (TOC) of silicon (~1.86×10^{-4} /°C) [95]. It is challenging to pursue an enhanced temperature sensitivity with the pure SOI material system compared to the reported results. Even integrated with

cladding materials having a high TOC, the guided mode in a silicon waveguide only partially interacts with the high-TOC materials, leading to a limited sensitivity.

One of the first silicon photonic temperature sensors was demonstrated using a silicon micro-ring resonator fabricated using a standard CMOS process [13]. The device consists of a ring and a bus waveguide with grating couplers at both ends. The measured sensitivity up to 0.083 nm/°C became the benchmark for comparing various silicon photonic temperature sensors. Another early silicon photonic temperature sensor based on a WBG was demonstrated with a reported sensitivity of 0.082 nm/°C [92], similar to the micro-ring resonator result. While having different advantages from their respective device configurations, both device configurations showed the bottleneck of the intrinsic temperature sensitivity of traditional silicon waveguide sensor designs using the SOI materials system.

To enhance the sensitivity of silicon photonic temperature sensors, the prior state-of-the-art devices incorporated advanced device configurations or cladding materials. By cascading two ring resonators with different radii, a silicon cascaded ring resonator sensor was reported to have a sensitivity of 0.294 nm/°C [90]. High sensitivity can also be realized in silicon MZI by tuning the widths and group indices of the two arms individually. With this method, a silicon photonic temperature sensor having a sensitivity of 0.438 nm/°C was demonstrated on an SOI platform with silica cladding [86]. For cladding materials other than traditional silica cladding in silicon photonics, devices integrated with negative TOC materials such as titania (TiO2) or SU-8 were demonstrated on an SOI platform. The measured temperature sensitivity of a titania cladded asymmetric silicon MZI temperature sensor was reported to be -0.340 nm/°C [87]. A silicon unbalanced MZI temperature sensor employing a silicon/SU-8 hybrid waveguide in one arm of the MZI showed a measured temperature sensitivity of 0.172 nm/°C [88]. In another example,

the silicon/SU-8 combination was implemented in a 2D photonic crystal waveguide temperature sensor with dual microcavities, and a sensitivity of 0.125 nm/°C was achieved by the simulation results [93].

Besides the negative TOC materials mentioned above, NLC materials are also promising for incorporation into optical waveguide temperature sensor devices, as the large TOC of NLC facilitates thermal sensing. Optical temperature sensors based on a silicon nitride (SiN) slot and double-slot ring resonators filled with NLC were proposed by Goncharenko et al. [96]. Their work numerically analyzed the dependence of device geometry, optical field distribution, and resulting temperature sensitivity. Wang. et al. demonstrated an optical temperature sensor based on a SiN ring resonator with NLC cladding and experimentally confirmed that approximately two orders of magnitude enhancement in temperature sensitivity can be achieved by incorporating NLC cladding [97].

However, unlike SiN waveguide devices, the larger refractive index and the stronger light confinement of silicon waveguides limit the enhancement in temperature sensitivity by introducing cladding materials with large TOC. To get stronger optical modal overlap with the cladding materials, SOI nano-meter slot waveguides with various geometries have been investigated for optical sensing applications after the invention by Almeida et al. in 2004 [21-22]. In SOI nano-slot waveguides, the quasi-TE mode is highly confined in the low-index gap between two closely and parallelly aligned silicon waveguides, offering ultra-compact and ultra-sensitive characteristics for optical waveguide temperature sensors [98]. Among the potential cladding materials with highly negative TOC, NLC is particularly favorable for SOI slot waveguides not only due to its high TOC (on the order of -1×10^{-3} /°C at T = 25°C in the direction of long molecular axis [37, 99-100]) but also due to its liquid nature which eases the

complete filling of the slot.

In this chapter, we propose a highly sensitive optical temperature sensor based on a silicon slot waveguide directional coupler with NLC cladding [36]. Two-mode interference within the slot region is induced naturally from a TE-polarized light input. Due to the difference in thermal-optical responses of the two modes, the output spectral transfer curve is shifted as ambient temperature changes. The high sensitivity comes from the combination of the large TOC of NLC cladding and strong light-matter interaction inside the slot region. Using the same device, two slot filling conditions, NLC (E7 made by Merck) and air, were used in separate rounds of characterization. In the following sections, we develop the theory of operation, introduce the device design and fabrication, present device results, and discuss the potential impact of this work.

4.2 Principle of operation and device design

The proposed optical temperature sensor relies on an SOI waveguide directional coupler cladded with NLC materials, shown in **Figure 4.1(a)**. TE-polarized light is launched into one arm of the device. In the active region, two silicon coupled-arm waveguides are brought close to each other, forming an NLC-filled nano-slot with a gap (width w_{slot}) between them. Light propagating in the active region can be considered as a linear combination of the TE0 and TE1 supermodes. The TE-like mode profiles of the symmetric TE0 mode and anti-symmetric TE1 mode are shown in **Figure 4.1(b)** and **Figure 4.1(c)**, respectively. While the TE0 mode has a strong overlap in the NLC-filled slot region, the TE1 mode has a minimum at the center of the slot region. As the ambient temperature T changes, the change in the refractive index of the NLC in the slot region dominates the change in the effective indices of both modes $n_{eff,s}$ and $n_{eff,a}$,

inducing a larger effective index difference in the TE0 mode than that of the TE1 mode. The distinct mode profiles of the two modes allow efficient modulation of the interference behavior. The two-mode interference and coupling length are therefore tuned by temperature, resulting in a lateral shift in spectral transfer functions measured at the outputs.

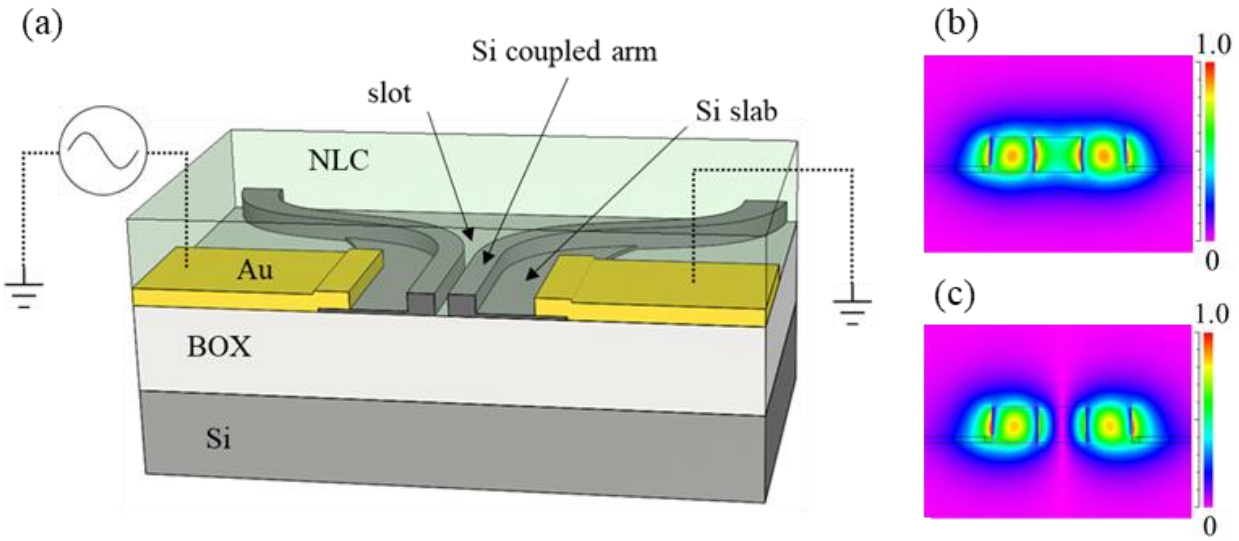

Figure 4.1: (a) Schematic of the proposed sensor showing a cross section at the slot waveguide region. An NLC cladding covers the active region and fills the nano-slot. (b) The TE0 mode profile and (c) the TE1 mode profile. They constitute the propagating supermodes in the slot waveguide region.

An NLC medium has strong birefringence. The refractive index of the media depends on the orientation of the rod-shaped NLC molecules. The long axes of NLC molecules align almost parallel to each other with a long-range order due to the presence of inter-molecule forces. The NLC material in the slot tends to be aligned parallel to the silicon slot waveguide due to the anchoring effect induced by the waveguide inner sidewalls [101]. The TE-like supermodes are influenced by the ordinary refractive index n_o of the slot NLC in this case. Efficient tuning of the slot NLC orientation by external electric fields is realized by introducing the strip-loaded slot

waveguide configuration into the directional coupler. The slot NLC molecules are aligned perpendicular to the slot waveguide through an external AC (alternating current) electric field applied through the two conductive silicon coupled-arm waveguides, allowing the optical fields to respond to the extraordinary refractive index n_e with higher TOC. The refractive index numbers of E7 used in simulations were obtained from the four-parameter model and fitting parameters reported in [37]. The results at 1550 nm wavelength as a function of temperature are illustrated in **Figure 4.2**, where <*n*> is the average refractive index calculated from

$$\langle n \rangle = \frac{(n_e + 2n_o)}{3} \qquad \textbf{(Equation 4.1)}$$

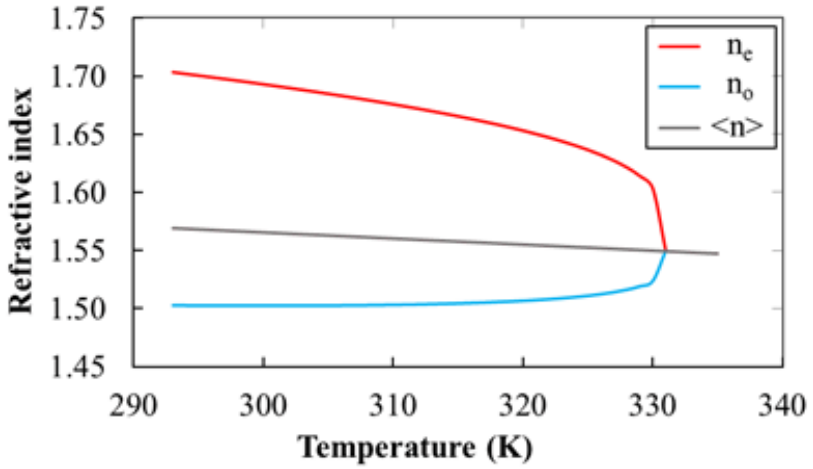

Figure 4.2: Temperature-dependent refractive indices of E7 at 1550 nm wavelength.

The temperature sensitivity of the proposed device can be derived and calculated from the two-mode interference and simulated effective indices $n_{eff,s}$ and $n_{eff,a}$ of a directional coupler. The effective indices were simulated from the cross section of silicon waveguide structure ($n_{Si,25°C}$ = 3.4803 with TOC = 1.86 × 10^{-4} /°C) on SiO_2 layer (n_{SiO_2} = 1.444 with negligible TOC) either cladded with air or E7. The parallel-state condition of a directional coupler can be written

as

$$L = m \cdot L_{cc} = \frac{m\lambda}{(n_{eff,s} - n_{eff,a})} \quad \textbf{(Equation 4.2)}$$

where L is the active length of the slot waveguide, m is the interference order (an integer for parallel state or a half-order for cross state), L_{cc} is the cross-coupling length of the directional coupler, and λ is the wavelength in vacuum. Including the wavelength dispersion effect, the m in **Equation 4.2** can be modified as [102]

$$m_{mod} = m - \left(\frac{\partial n_{eff,s}}{\partial \lambda} - \frac{\partial n_{eff,a}}{\partial \lambda}\right) \cdot L \quad \textbf{(Equation 4.3)}$$

The refractive index variation of silicon due to thermal expansion (3.57×10^{-6} /°C) [86, 91] is much smaller than that due to the thermal optic effect (1.86×10^{-4} /°C). Although the thermal expansion was reported to be able to cause molecular reorientation of NLC materials [103], the applied electric field is assumed large enough (i.e., above saturation) to maintain fully aligned NLC molecules. Thus, the thermal expansion effect is ignored in the following analysis. The temperature sensitivity S, defined as the wavelength shift over a temperature change, can be expressed as $\partial\lambda/\partial T$. From the above expressions, the sensitivity S relationship can be derived as

$$S = \frac{\partial \lambda}{\partial T} = \frac{L}{m_{mod}} \cdot \left(\frac{\partial n_{eff,s}}{\partial \lambda} - \frac{\partial n_{eff,a}}{\partial \lambda}\right) = \frac{\lambda}{(n_{g,s} - n_{g,a})} - \left(\frac{\partial n_{eff,s}}{\partial T} - \frac{\partial n_{eff,a}}{\partial T}\right) \quad \textbf{(Equation 4.4)}$$

where n_g is the group index given by $n_g = n_{eff} - \lambda \cdot (\partial n_{eff}/\partial \lambda)$, and $n_{g,s}$ and $n_{g,a}$ are the group indices of the symmetric TE0 mode and anti-symmetric TE1 mode, respectively. The temperature sensing is a result of the different responses of the two modes, based on a combined effect of the wavelength and temperature dependence. The operation is similar to the case of a silicon MZI waveguide sensor [86], having the temperature sensing based on the different response of the two fundamental modes guided in the two arms. However, for the proposed directional coupler device, the two-mode interference occurs in the same slot waveguide,

narrowing down the lateral size of the sensor.

To have a further physical picture of the proposed device, the sensitivity *S* can be combined with other properties of the directional coupler device. The free spectral range (FSR) of the directional coupler can be calculated using the following equation

$$FSR = \frac{\lambda^2}{L \cdot |n_{g,s} - n_{g,a}|} \quad \textbf{(Equation 4.5)}$$

which illustrates the wavelength dependence of the device. The value of FSR/2 can be viewed as the wavelength change required for full switching of the propagating light from one coupled-arm waveguide to the other. Comparably, fixing the wavelength, the temperature change needed for full switching is defined as T_π. To derive an expression for T_π, one can start with the switching condition

$$\left| \frac{L}{L_{cc}(T)} - \frac{L}{L_{cc}(T+T_\pi)} \right| = 1 \quad \textbf{(Equation 4.6)}$$

Substituting L_{cc} in Eq. (1) into Eq. (5), T_π can be derived as:

$$T_\pi = \frac{\lambda}{2L \cdot \left| \frac{\partial n_{eff,s}}{\partial T} - \frac{\partial n_{eff,a}}{\partial T} \right|} \quad \textbf{(Equation 4.7)}$$

Substituting **Equation 4.5** and **Equation 4.7**, both the wavelength dependence and temperature dependence, into **Equation 4.4**, the expression for *S* can be obtained as

$$|S| = \frac{FSR}{2T_\pi} \quad \textbf{(Equation 4.8)}$$

Equation 4.8 shows that the sensitivity *S* of the proposed sensor is independent of the active length *L* since both FSR and T_π are inversely proportional to *L*.

The sensing range ΔT_r of such devices based on wavelength shift over temperature is defined as the temperature range between two troughs in the spectral transfer curves. It can be specified by either FSR/|*S*| or $2T_\pi$. Thus,

$$\Delta T_r = 2T_\pi = \frac{FSR}{|S|} = \frac{\lambda}{2L \cdot \left| \frac{\partial n_{eff,s}}{\partial T} - \frac{\partial n_{eff,a}}{\partial T} \right|} \quad \textbf{(Equation 4.9)}$$

Unlike the sensitivity *S*, the sensing range ΔT_r can be engineered with active length *L* based on the requirements of the specific application.

4.3 Device fabrication

The fabrication process flow of the proposed sensor is generally the same as the EO switch described in Chapter 3 but with some differences in the slot waveguide geometry. The slot width is wider in the temperature sensor to have a larger sensing region, as the voltage applied is not a major consideration in this case. The NLC molecules are set to stay the same alignment condition during sensing. Since the sensor working principle does not rely on molecule reorientations, the slot region of the sensor does not employ a significant overetch.

The fabrication process is illustrated by a simplified schematic process flow in **Figure 4.3(a)-(j)**. The silicon waveguide structures were fabricated using two steps of electron-beam lithography patterning followed by RIE using SF6:CHF3 plasma on an SOI wafer with a 250 nm thick Si device layer and a 3 µm thick SiO_2 buried layer. Within the 1.5 mm long slot region, the measured slot width is 310 nm, and the waveguide width is 300 nm for both coupled arms. The slot waveguides are connected to 45 nm thick silicon slabs to facilitate electrical contacts. The slot waveguides and slabs were doped with phosphorus to be n-type. A 2 µm SiO_2 layer is deposited by PECVD on top of the waveguides. The slot region was opened through a combination of RIE and BOE. Gold contact pads were formed by sputtering and then lift-off process to connect to the conductive silicon slabs separately. A top-view image of the device at this stage taken with an optical microscope is shown in **Figure 4.3(k)**. Finally, NLC was applied to the slot region.

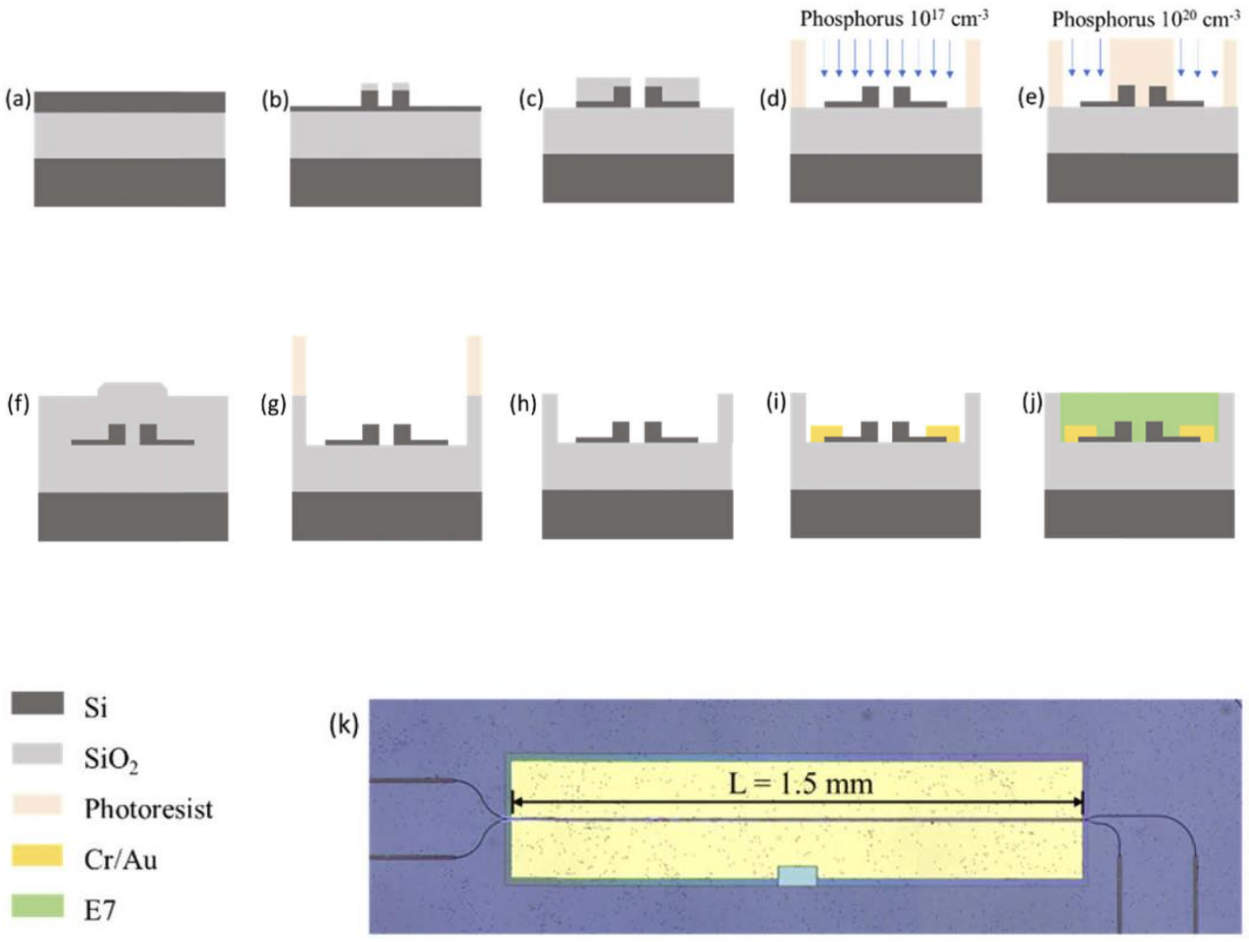

Figure 4.3: (a)-(j) Schematic representation of the fabrication flow of the proposed sensor. (k) Optical microscope image of the fabricated silicon slot waveguide directional coupler before NLC infiltration at the slot region.

4.4 Experimental results

The device was tested with an air-cladded slot first before the NLC was applied on top of it. The temperature-dependent transmission spectra measured from one of the output ports are shown in **Figure 4.4**. Temperature sensitivity is extracted from the slope of the linearly fitted trough wavelength shifts over temperature changes. The measured temperature sensitivities are 0.110 nm/°C at room temperature and 0.123 nm/°C with temperatures above 50°C. The

temperature dependence for the air-cladded device is dominated by the TOC of silicon, showing similar results for both temperature ranges. There are Fabry-Perot effects from internal reflections within the device shown in the measured spectra. The ripples may not be fully revealed due to under-sampling limited by our discrete stepper tunable laser.

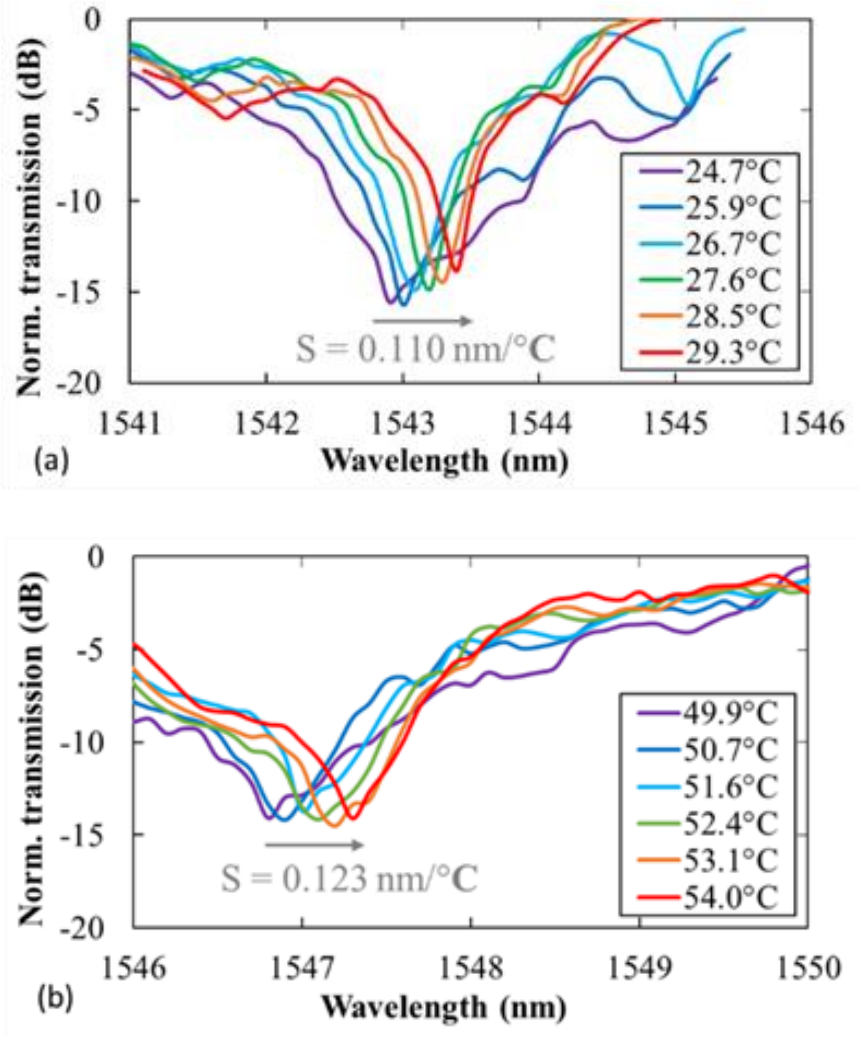

Figure 4.4: Optical spectral responses of the air-cladded sensor (a) at room temperatures and (b) above 50°C.

E7 is the NLC material used to infiltrate the slot waveguide on the same device for another characterization round. A 10 V square-wave AC voltage at 5 kHz frequency was applied across the NLC cladded device during the measurements. **Figure 4.5** shows the spectra results of the E7-filled sensor around room temperature and slightly below the clearing temperature, the phase transition point between liquid crystal and isotropic liquid. For the E7-cladded case, the extracted temperature sensitivities are 0.810 nm/°C at room temperature and 1.619 nm/°C from 50.1°C to 52.0°C. In **Figure 4.5(a)**, the trough shapes evolve gradually as the temperature increases. The liquid crystal nature makes the material susceptible to local defects and fabrication imperfection. The microscopic direction of NLC molecules around defects can be different from the macroscopic behavior and is temperature-dependent. As the temperature is raised, the TOC of E7 for n_e becomes higher until reaching the corresponding clearing temperature (58°C for E7 [37]). This temperature dependence in the NLC materials leads to higher sensitivity at a temperature close to and below the clearing temperature. When the ambient temperature is higher than the clearing temperature, the NLC changes from nematic to isotropic phase. The respective TOC is no longer high and useful for temperature sensing applications. In other words, the incorporated NLC's clearing temperature defines the upper limit of the operational temperature of the proposed sensor.

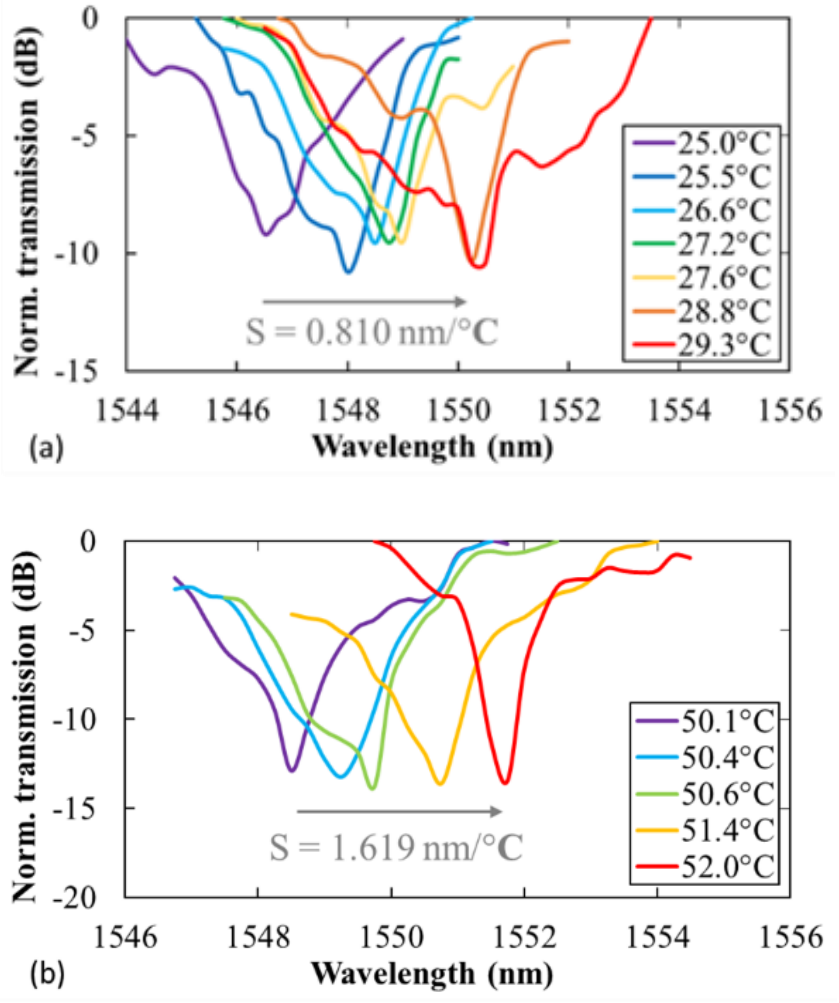

Figure 4.5: Optical spectral responses of the NLC(E7)-infiltrated sensor (a) at room temperatures and (b) above 50°C.

The results of trough wavelength shift with respect to temperature are summarized in **Figure 4.6**. It is shown that the temperature sensitivities are enhanced by around one order of magnitude with E7 incorporated into the device. The standard error of estimate (SEE) values for the four conditions were calculated and converted to temperature using the extracted slopes. For the air-cladded condition, the SEE values are 0.12°C around room temperature and 0.05°C above 50°C. For the E7-filled condition, the SEE values are 0.31°C around room temperature and

0.12°C above 50°C. To test the stability and repeatability of the measurements, the E-7 filled sensor was measured ten times at 27°C and 51°C, respectively. The standard deviation (SD) results are 0.027 nm at 27°C and 0.150 nm at 51°C. The fluctuations in temperature calculated from the SD and corresponding S are 0.03°C at 27°C and 0.09°C at 51°C. The higher SEE for the E-7 filled condition around room temperature is thus attributed to the liquid crystal in the slot, consistent with the spectra shape distortion in **Figure 4.6(a)**. The sensitivity of the measured device is expected to be even higher than 1.619 nm/°C as the temperature goes higher and closer to the clearing temperature of E7. However, the temperature gradient of n_e at that temperature range is highly nonlinear, making it harder to extract accurate sensitivity numbers using linear fitting.

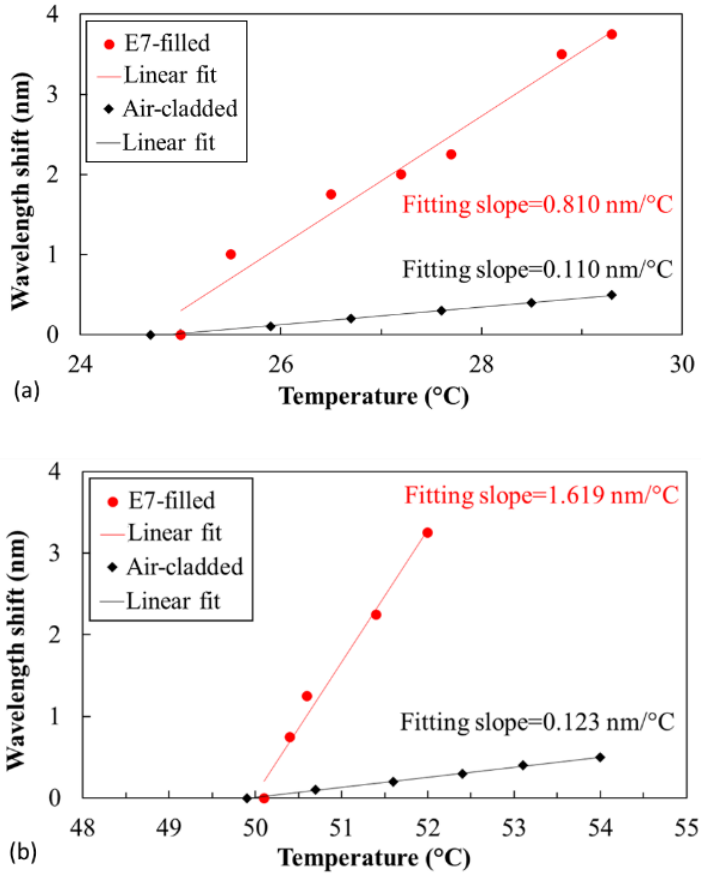

Figure 4.6: Measured wavelength shift with temperature for the air-cladded and E7-filled device conditions (a) at room temperatures and (b) above 50°C.

Based on the simulated effective indices $n_{eff,s}$ and $n_{eff,a}$ of the fabricated device structure, the S values in a given temperature range can be calculated with **Equation 4.4**. The measured sensitivities and the corresponding simulated results are listed in **Table 4.1**. For the E7-filled case, the sensitivities between the two temperature ranges investigated are expected to follow the trend of E7's TOC ($dn_e/d\lambda$), which can be calculated from the results in **Figure 4.2**.

Table 4.1: Measured and simulated sensitivities of the fabricated sensor device.

Slot condition	Experimental		Simulated		Error (%)
	Temp. (°C)	Sensitivity (nm/°C)	Temp. (°C)	Sensitivity (nm/°C)	
Air-cladded	24.7-29.3	0.110	27	0.108	1.8
	49.9-54.0	0.123	51	0.114	7.8
E7-filled	25.0-29.3	0.810	27	0.741	9.3
	50.1-52.0	1.619	51	1.845	12.2

The sensing range ΔT_r, related to the device FSR, has been investigated. **Figure 4.7** shows the measured spectra in broader wavelength ranges and the measured FSR corresponding to the four sample conditions. For the air-cladded condition, the FSR is ~6.2 nm at 24.9°C, similar to the measured ~6.1 nm at 52.4°C. After E7 filling, the FSR was measured to be ~4.5 nm at room temperature. At 52.0°C, the E7-filled device showed an even lower FSR of ~3.8 nm. This corresponds to a maximum ΔT_r of 5.6°C for the E7-filled sensor. To obtain a more significant ΔT_r, one can increase the FSR by decreasing the active device length L or changing the waveguide geometry. However, there exists a trade-off between FSR and spectral resolution. The optical loss through the sensor has also been measured. The sensor has ~7.4 dB insertion loss in the 1.5 mm-long device region for both air- and E7-cladded conditions. We expect the

device insertion loss can be reduced by improvement in fabrication processes such as reducing sidewall roughness and optimizing doping profiles.

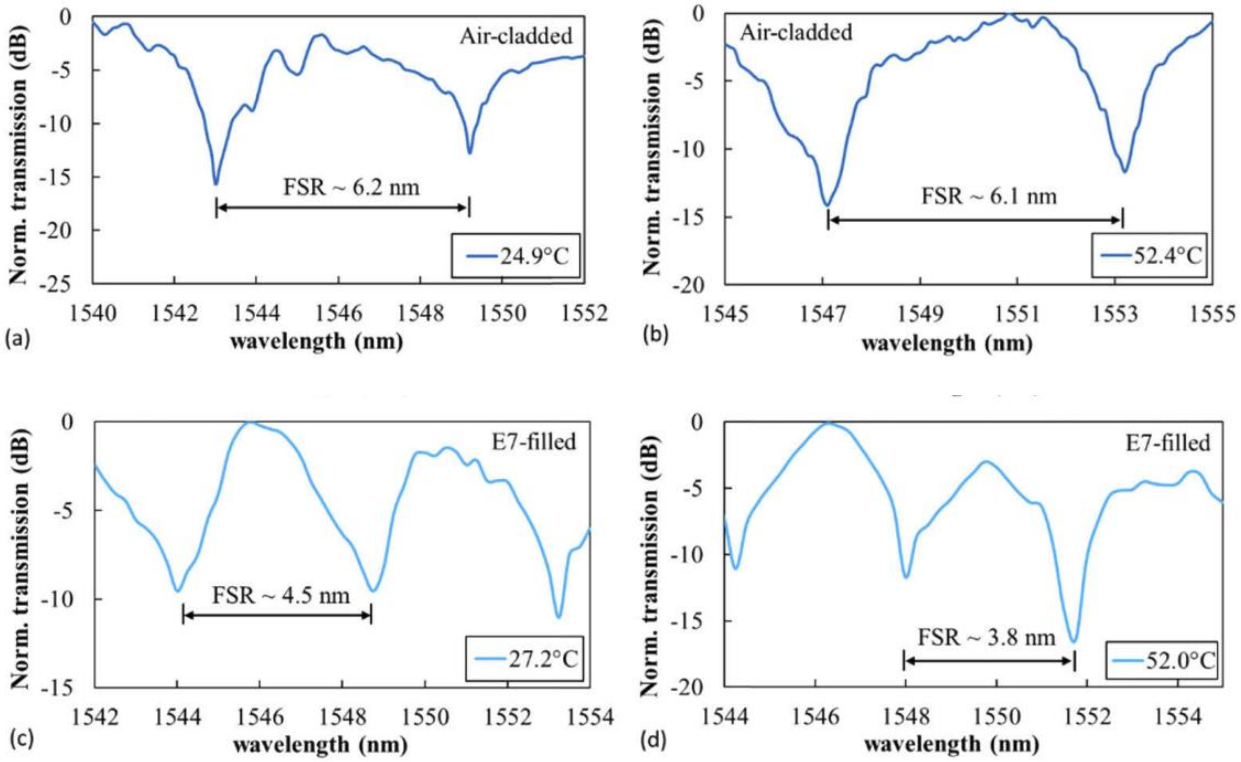

Figure 4.7: Optical spectral responses of the air-cladded sensor (a) at 24.9°C and (b) at 52.4°C and and NLC(E7)-infiltrated sensor (c) at 27.2°C and (d) at 52.0°C.

4.5 Discussion

This section discusses the NLC material selection and orientation control for the proposed sensor. Then the advantages of using a directional coupler configuration over an MZI configuration are raised.

4.5.1 NLC material

It is worth noting that the NLC material for the proposed sensor is not limited to the one used in the demonstrations. E7 is a widely used and easily obtained option for initial demonstrations. The NLC material for the device configuration can be flexibly chosen based on application requirements. For example, compared to E7, some other NLC options listed in [100] exhibit a larger temperature gradient of n_e. The proposed temperature sensor could be even more sensitive if one of those NLC materials was chosen to be applied. However, the clearing temperatures are generally lower for high temperature-gradient refractive index NLCs, suggesting a trade-off between sensitivity and operational temperature range originating from the NLC material to be incorporated. Generally, NLC materials with both high TOC and a wide operational temperature range are ideal candidates for the proposed sensor.

4.5.2 NLC molecule orientation control

The performance of the sensor is highly dependent on the NLC molecule orientation. Since n_e provides for a larger TOC than n_o, the highest sensitivity occurs when the NLC molecules are fully aligned perpendicular to the slot waveguide direction. It is demonstrated in [40] that saturation in phase shifts was observed by measuring the electro-optically induced phase shifts over the applied voltage of AC signals. The saturation effect in phase shifts was due to wholly reoriented NLC molecules in the slot region. Similarly, efficient NLC reorientation is facilitated in this work by confining the applied electric field across the nano-slot. At room temperature, phase shifts in the device saturate with a 7 V square-wave AC signal at 5 kHz. Therefore, a 10 V square-wave AC signal with a frequency of 5 kHz was used during temperature sensing measurements to maintain the same fully aligned condition over temperature

changes. The saturation voltage of the device can be lowered by optimizing the slot waveguide geometry, e.g., reducing the slot width or introducing an overetch in the slot [63].

Although electrical control was successful in horizontal NLC alignment for the sensing demonstration, it is not ideal. The active control method requires extra power consumption and control electronics [63]. Implementing a passive NLC alignment method is preferable and is one of the future directions of this sensor work.

4.5.3 Advantages over the MZI configuration

The sensing mechanism of the proposed directional coupler sensor relies on the different temperature responses of the two guided modes, which is similar to that of MZI-based sensors in a general form. However, the proposed directional coupler sensor confines the two naturally launched TE modes in only one slot waveguide region. The two modes sense from within the same waveguide structure and in the same thermal environment. Any irregularities in the slot waveguide region contribute to both modes, leading to more spatially precise and consistent sensing results. Since the sensed area is assumed to be uniform in temperature, having only one sensing arm is better in terms of spatial resolution than having two arms. The sensing of the proposed directional coupler temperature sensor is dominated by the TO effect of NLC material inside the slot region with 310 nm width. This characteristic gives the directional coupler sensor a fundamental advantage of sub-micrometer level one-dimensional (1D) spatial resolution in the direction perpendicular to the slot waveguide. The superior 1D spatial resolution makes the sensor a great candidate for potential applications such as regional on-chip temperature monitoring and precise 1D temperature mapping using a sensor array.

4.6 Conclusion

We have theoretically analyzed and experimentally demonstrated an NLC filled silicon nano-slot waveguide photonic temperature sensor with high sensitivity and submicron 1D spatial resolution. The measured sensitivities for the E7-filled two-mode interference device are 0.810 nm/°C around room temperature and 1.619 nm/°C from 50.1°C to 52.0°C, showing good agreement with the simulated results. Combining the strong light-matter interaction from slot waveguide and the high TOC of NLC, the experimentally achieved sensitivity represents the highest achieved for silicon waveguide-based temperature sensors at the time [36] was published. The demonstrated sensor is flexible in the NLC material selection to meet the sensitivity and operational temperature range requirements for specific applications.

4.7 Acknowledgement

Chapter 4, in full, is a modified reprint of Li-Yuan Chiang, Chun-Ta Wang, Ting-Syuan Lin, Steve Pappert, and Paul Yu, "Highly sensitive silicon photonic temperature sensor based on liquid crystal filled slot waveguide directional coupler," *Opt. Express* **28**, 29345-29356 (2020) with additional details. The dissertation author was the primary investigator and author of this material. I would like to acknowledge the Office of Naval Research (ONR) (contract N00014-18-I-2027) for the support of this work.

Chapter 5

A power-efficient thermo-optic (TO) switch

5.1 Introduction

Silicon photonic switching has been perceived as a promising technique for optical communication [1, 9, 104], LiDAR [2, 49, 105], and programmable photonic integrated circuit (PIC) [6, 106] applications. Among different types of optical switches, TO switches offer low optical loss and a relatively simple fabrication process. However, the TO efficiency remains an issue. Although silicon has a large TO coefficient ($dn/dT \sim 1.86 \times 10^{-4}$ K^{-1} at 1.55 μm wavelength), there is unwanted thermal spreading inherent in TO switch devices, leading to inefficient heating and large power consumption (usually $P_\pi \sim$ 10 - 30 mW). Most switching applications require cascaded switch topologies and many switch elements, but TO switches' power-hungry characteristic limits the total number of elements that can be integrated. It is also challenging to realize a compact design (< 100 μm in length) and simultaneously achieve small switching voltage V_π and low thermal crosstalk.

Air trenches/cavities can be introduced to TO actuators to improve TO efficiency and achieve low power consumption, but with a tradeoff of slower response time [107]. Another strategy is to utilize materials with a higher TO coefficient than silicon. By incorporating nematic liquid crystals (NLC) into a slot waveguide directional coupler, the TO response was enhanced by ~10 times [36]. However, the requirement of an external electric field for NLC alignment in the slot complicates the control, making it harder to be implemented in TO

switches. Electric driving also requires additional power consumption, reducing the benefit of a stronger TO response from the NLC.

In this work, we propose a silicon directional coupler TO switch with enhanced efficiency enabled by passively aligned NLC [108]. The passive alignment method replaces the active alignment, as mentioned in Chapter 4. The proposed passive alignment method simplifies the fabrication process and avoids the extra power consumption from an external electric field. Subwavelength gratings (SWGs) [109-111] are integrated to provide for the passive alignment through the physical constraints at the sidewalls [112]. The periodic gratings were sensed effectively as a conventional dielectric medium during light propagation in the subwavelength regime. The diffraction effect from the periodic structures is suppressed in the subwavelength regime, enabling low-loss propagation with the grating structures. By incorporating SWGs and NLC into our slot directional coupler TO switch, we demonstrated that the TO efficiency and power consumption can be significantly improved without sacrificing the response time.

5.2 Principle of operation and device design

A schematic of the proposed directional coupler TO switch is shown in **Figure 5.1**. It is based on a strip-loaded slot waveguide with nano-grooves formed by SWGs inside the slot [108]. A portion of the silicon slabs was n-doped ($10^{20}/cm^3$) to form heaters. In the n-doped slabs, there are four square regions connected with gold contact pads. The slot waveguide and a portion of silicon slabs remain undoped to minimize the propagation loss due to impurity scattering and carrier injection. The chip is covered with SiO_2 cladding, except for the device region. NLC materials, E7 and 5CB (made by Merck), were used on separate dies of devices for testing. After applying an NLC cladding on a device, the NLC molecules filled the slot with the molecular

orientations aligned by the nano-grooves [108, 112]. The aligned NLC molecules have their long axes parallel to the SWGs.

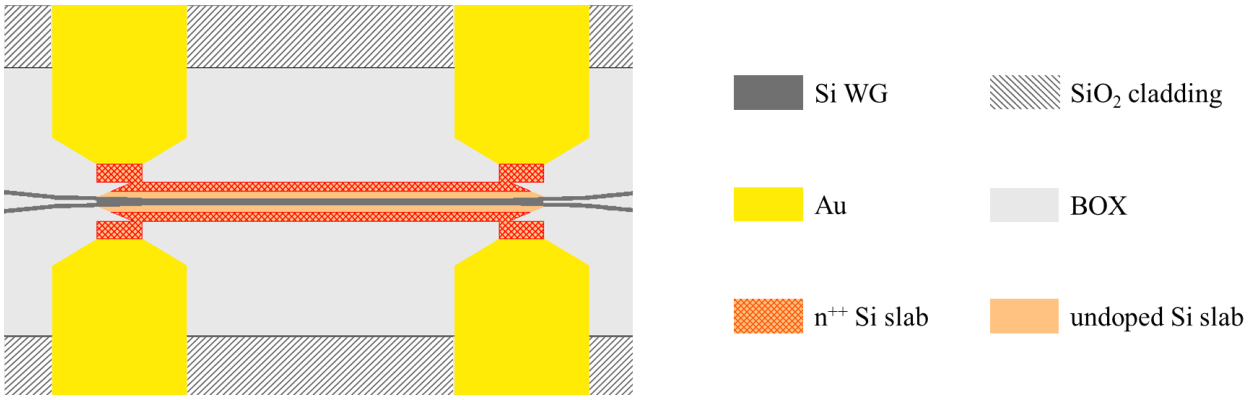

Figure 5.1: Schematic top-view of the proposed device before applying NLC.

The device was operated with a TE-polarized input at 1550 nm. Two supermodes are launched at the directional coupler with a heat-sensing hotspot along the slot region [36]. The TE modes probe the extraordinary refractive index of the NLC molecules in the nano-grooves and sense the large TO coefficient (dn_e/dT on the order of -1×10^{-3} K^{-1} at 1.55 μm wavelength for E7 and 5CB). The TO switching is realized by changing the temperature of the slot waveguide and the NLC. The temperature change ΔT induces material index changes Δn and consequently effective mode index changes Δn_{eff}. In other words, the proposed device relies on the TO effect of NLC instead of the NLC reorientation described in Chapter 3. Electric current flows through the heaters can generate heat to change the temperature. The electrical power consumption required is calculated by V^2/R, where V is the voltage applied, and R is the total resistance of the heaters.

A schematic cross-section view of the slot region is shown in **Figure 5.2**. The heaters

have a certain distance (width of the undoped silicon slabs) away from the slot waveguide arms for low-loss light propagation. The undoped silicon slabs facilitate heat transfer of the slot waveguide for both heating and cooling due to the substantial thermal conductivity of silicon. With the effective heat transfer and strong TO effect from the NLC, the power consumption of switching is thus significantly reduced.

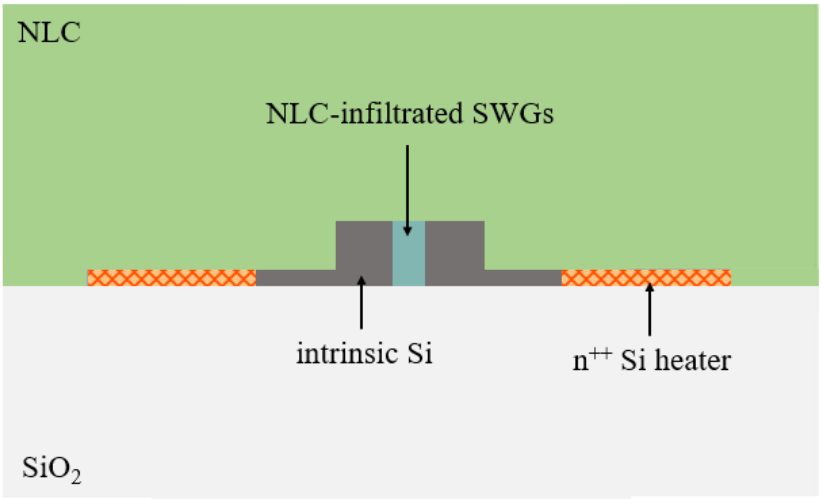

Figure 5.2: Cross-section schematic of the proposed TO switch based on an SOI strip-loaded slot waveguide and two n^{++} silicon heaters.

The figure of merit (FOM) for TO switches is usually defined as the power-time product [113, 114] with the following equation

$$\mathrm{FOM} = P_\pi \cdot \tau = \Delta T_\pi \cdot H \qquad \textbf{(Equation 5.1)}$$

where P_π is the power consumption to reach one full on/off switching, τ is the limiting time constant either from the heating or cooling process, ΔT_π is the temperature change required for one complete switching, and H is the heat capacity of the heated arm. The P_π and τ can be formulated as

$$P_\pi = \Delta T_\pi \cdot G \cdot A \quad \textbf{(Equation 5.2)}$$

$$\tau = \frac{H}{G \cdot A} \quad \textbf{(Equation 5.3)}$$

where G is the thermal conductance between the heated silicon structures and the heat sink (silicon substrate in this case), and A is the traversed area for the heat flow. Although the power consumption P_π may be lowered by having a smaller product of G and A, this does not result in a better FOM due to the counterbalancing from a larger τ. From the above equations, lowering ΔT_π or H values is essential to getting a lower FOM and better performance.

The ΔT_π can be written as

$$\Delta T_\pi = \frac{\lambda_o}{2L \cdot \frac{dn}{dT}} \quad \textbf{(Equation 5.4)}$$

where λ_o is the free-space wavelength, L is the switch device length, and dn/dT is the thermo-optic coefficient (TOC). Whereas ΔT_π is inversely proportional to L from **Equation 5.4**, both A and H are directly proportional to L. The P_π, τ, and FOM are independent of the device length L. In this work, we utilize the high TOC of NLC to lower the ΔT_π of the device. Other parameters such as G, A, and H are dominated by the SOI waveguide structures with no significant counterbalancing. Thus, the overall FOM can be improved with the proposed technique.

To support low-loss waveguiding, the gratings in the slot need to be in the subwavelength regime [109-111]. The subwavelength condition can be written as

$$\lambda \gg \lambda_B = 2 \cdot n_{eff} \cdot \Lambda \quad \textbf{(Equation 5.5)}$$

where λ_B is the Bragg wavelength where Bragg reflection occurs, and Λ is the pitch of the gratings. In a subwavelength regime, λ_B is much smaller than λ. This is usually realized by having a small pitch Λ. The pitch of the SWGs was designed to be <150 nm in this work. The n_{eff} of the modes are ~2. The approximate λ_B is below 600 nm, fulfilling the subwavelength condition represented in **Equation 5.5**.

5.3 Device fabrication

The fabrication process flow of the proposed TO switch is similar but with fewer steps than the temperature sensor described in Chapter 4. The TO switch only went through one ion implantation step to form the heaters. The slot waveguide is kept intrinsic to possess lower scattering loss and better thermal conductivity [111]. The SWGs in the slot region were formed along the slot waveguide, requiring no additional fabrication step.

The fabrication process is illustrated by a simplified schematic process flow in **Figure 5.3**. The silicon waveguide structures were fabricated using two steps of electron-beam lithography patterning followed by RIE using SF6:CHF3 plasma on an SOI wafer with a 250 nm thick Si device layer and a 3 μm thick SiO_2 buried layer. The slot waveguides are connected to 50 nm thick silicon slabs. The outer parts of the slabs were heavily doped with phosphorus to be n^{++} silicon heaters. Each heater is connected with square slabs at both ends for metal contacts. A 2 μm SiO_2 layer is deposited by PECVD on top of the waveguides. The slot region was opened through a combination of RIE and BOE without a significant overetch. Gold contact pads were formed by sputtering and then lift-off to connect to the silicon square slabs separately. NLC was applied to the slot region as the final step.

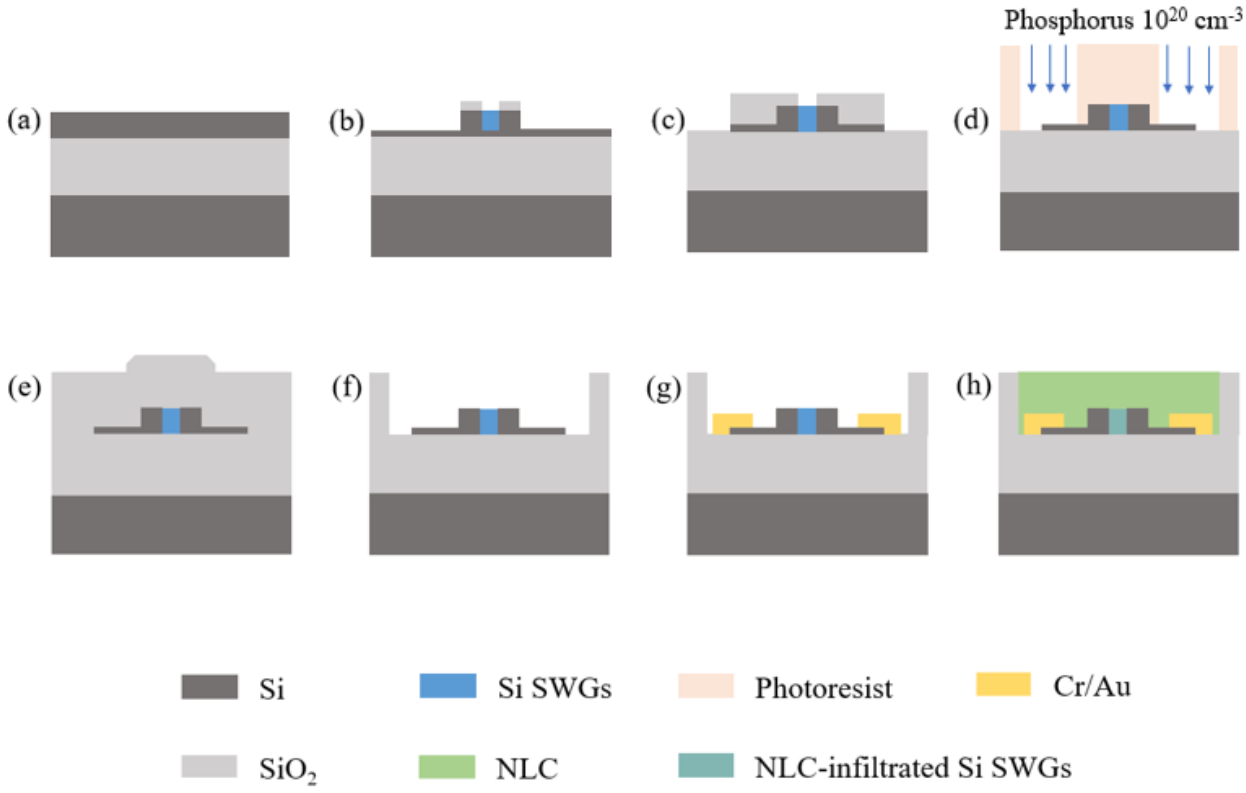

Figure 5.3: Schematic representation of the fabrication flow of the proposed TO switch.

SEM top-view images of a fabricated TO switch before NLC infiltration are shown in **Figure 5.4**. The square slab regions (5 µm on each side) are designed for reliable photolithography alignment during metal contacts formation. At both the input and output sides of the directional coupler, the slot waveguide and slabs have a 5 µm long tapering region for proper optical mode transition. The zoomed-in SEM image in **Figure 5.4** displays the SWGs in the slot region. The SWG structures have the same height as the slot waveguide arms. The SWGs are perpendicular to the slot waveguide direction, forming nano-grooves which are nearly rectangular. The shape of the nano-grooves plays an essential role in the NLC alignment, and a larger aspect ratio of the width to length is desirable for better alignment effect [115].

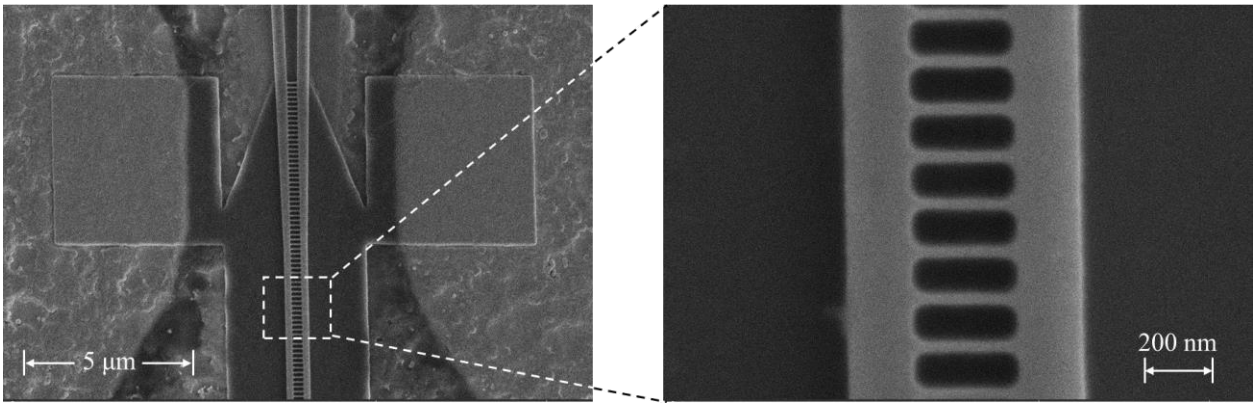

Figure 5.4: SEM images of a fabricated TO switch before NLC infiltration at the slot region.

Optical microscope images of a fabricated device before applying NLC are shown in **Figure 5.5**. Two square metal pads were formed for probing and applying electrical current. Each metal pad was connected to two silicon square slabs. The metal lines mainly lie on top of the 2 μm SiO_2 cladding. Although there are four crossing parts between the metal lines and silicon waveguides, the optical loss induced is negligible due to the separation in the vertical direction. Since the SiO_2 cladding on the device region was etched to reveal the slot waveguide, the metal lines need to cover a 2 μm step height without breakage. Thus, the metal layer was deposited by sputtering to ensure good step coverage.

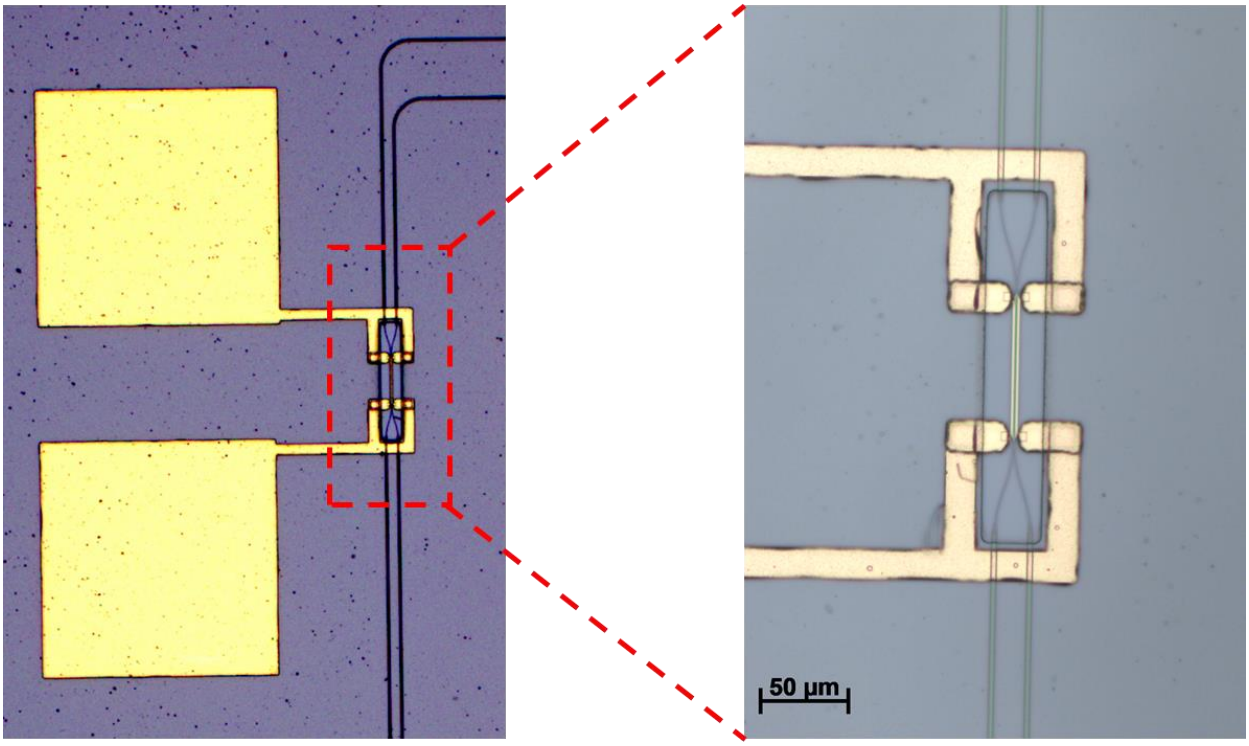

Figure 5.5: Optical microscope images of the fabricated TO switch before NLC infiltration at the slot region.

5.4 Results – E7 TO switch

The E7 device was designed to be 40 µm long, with additional 5 µm long tapered regions at both the input and output sides. The waveguide width of the silicon coupled arms is 210 nm. The pitch and silicon filling factor of the gratings in the slot are 140 nm and ~0.286, respectively. The corresponding Bragg wavelength is ~560 nm which is much lower than the operating wavelength 1550 nm to ensure the subwavelength and low-loss propagation in the device [109]. The nano-grooves have an aspect ratio of 3 (~100 × 300 nm^2). E7 is the NLC material used to fill the nano-grooves.

The optical performance was measured from one of the output ports in the directional coupler switch. As shown in **Figure 5.6**, TO switching was demonstrated by electrically driving

the two heaters in parallel with a measured total resistance of 7.9 kΩ. The electrical power consumption P_π is 3.7 mW, with a corresponding extinction ratio of ~16 dB. The transmission slope became sharper when the power was increased up to the OFF state due to the higher TOC of the NLC at that higher-temperature range. As the power was increased beyond ~5.3 mW, the transmission curve turned flat. In this region, the slot temperature is higher than the clearing temperature of the NLC. The NLC material becomes the isotropic phase and does not possess a large TOC. The phase transition is reversible. After measuring the transmission curve and calibrating the operating voltage/power values, the NLC material was kept in the nematic phase while operating the switch.

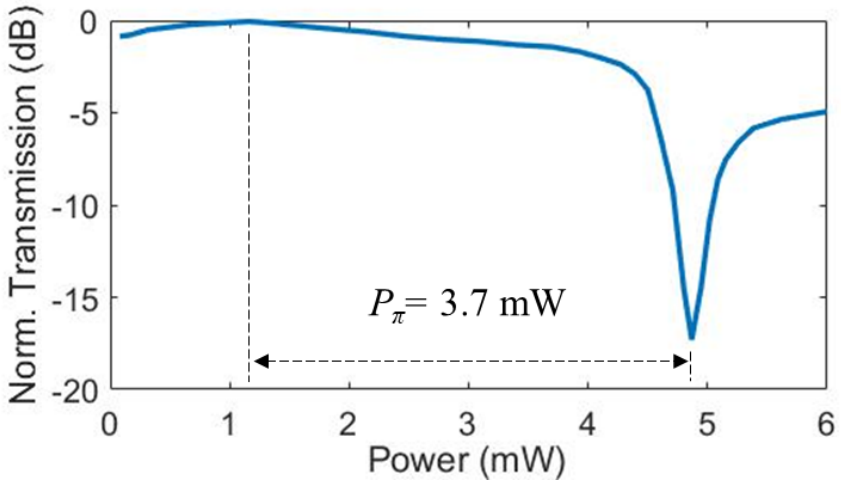

Figure 5.6: The measured optical transmission results as a function of power applied from the E7 TO switch.

The temporal responses, shown in **Figure 5.7**, were recorded as the device was periodically switched between the ON and OFF states with a square-wave driving signal at 5 kHz. The cooling (rise) time constant $\tau_{cooling}$ and heating (fall) time constant $\tau_{heating}$ measured are 5.4 μs and 10.7 μs, respectively. Unlike most NLC devices relying on controlling the

reorientations of NLC molecules and having response time in millisecond-level [40, 58, 63], the speed of the Si-NLC hybrid TO switch depends on the thermal properties of both silicon and the NLC material incorporated. The slower $\tau_{heating}$ is as expected due to the nonlinear TO coefficient of NLC and the inducing nonlinear TO response of the switch. As shown in the transfer curve in **Figure 5.6**, the transmission slope became sharper when the power was increased up to the OFF state. As a result, the heating process requires a more considerable temperature change to reach the signal level defined from τ. The FOM calculated for the E7 device is 39.6 nW·s.

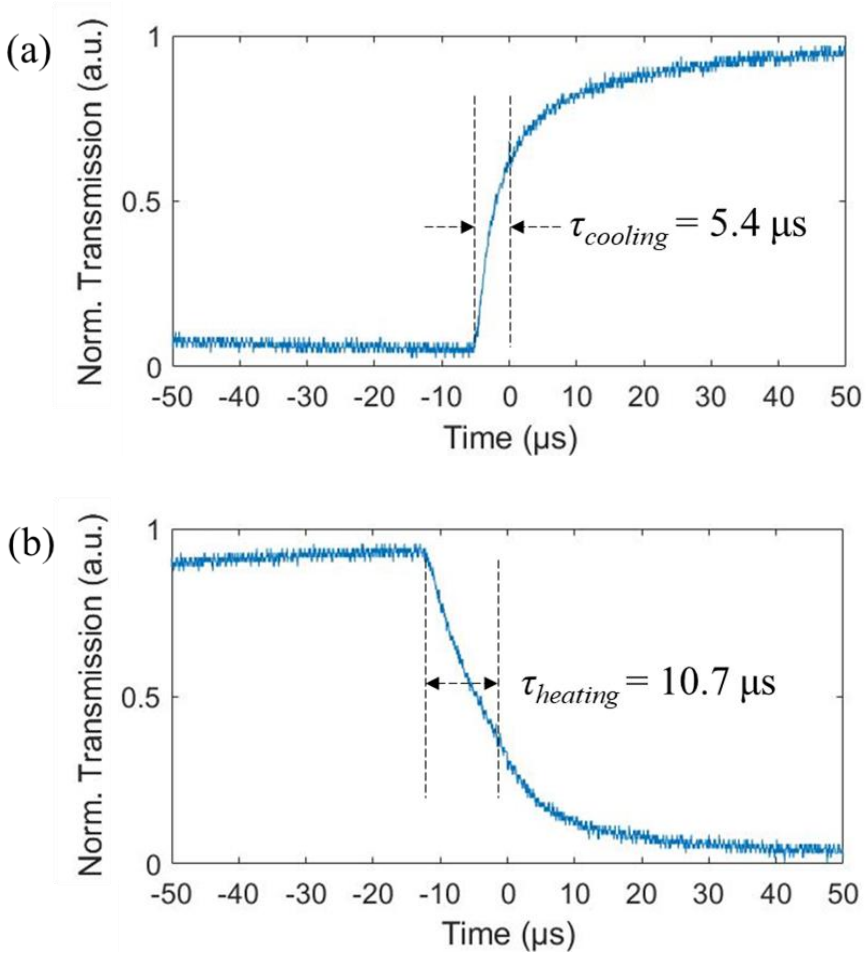

Figure 5.7: Measured temporal responses of the E7 TO switch for (a) switching ON (cooling) and (b) switching OFF (heating).

5.5 Results – 5CB TO switch

5CB is an NLC having similar material properties as E7 but with larger TOC values and a smaller nematic temperature range than E7. The extraordinary refractive indices of E7 [37] and 5CB [116] at 1550 nm wavelength are plotted in **Figure 5.8**. The 5CB device was designed as L = 80 μm, which is longer than the E7 device. The longer L causes a smaller ΔT_{π}, enabling the switching to be operated only in the large-TOC temperature range. There are additional 5 μm long tapered regions at both the input and output sides. The measured waveguide width of the silicon coupled arms is 210 nm. The pitch and silicon filling factor of the gratings in the slot are 105 nm and ~0.286, respectively. The corresponding Bragg wavelength is ~420 nm, much lower than the operating wavelength 1550 nm to be in the subwavelength regime. The nano-grooves have an aspect ratio of 4 (~75 × 300 nm^2).

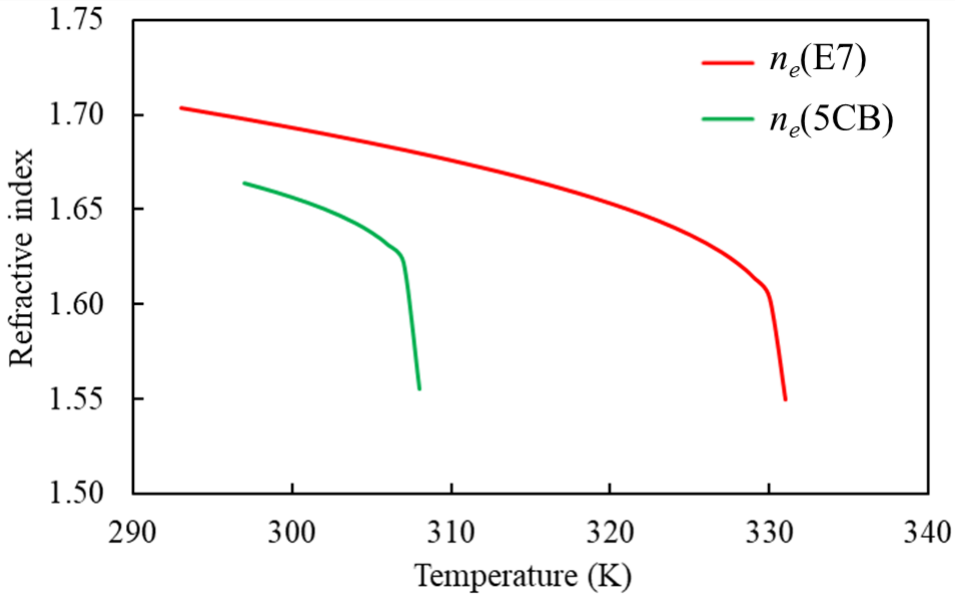

Figure 5.8: Temperature-dependent extraordinary refractive indices of E7 and 5CB at 1550 nm wavelength.

The optical performance was measured from both output ports in the 2×2 directional coupler switch and plotted in **Figure 5.9**. The electrical power consumption P_π is only 0.58 mW. The extinction ratios are >22 dB. The measured total resistance is 10.7 kΩ, and the corresponding V_π is 0.57 V. Both transmission curves match decently in the ON/OFF states. The 5CB became isotropic with flat transmission curves as the power was increased beyond ~3.2 mW.

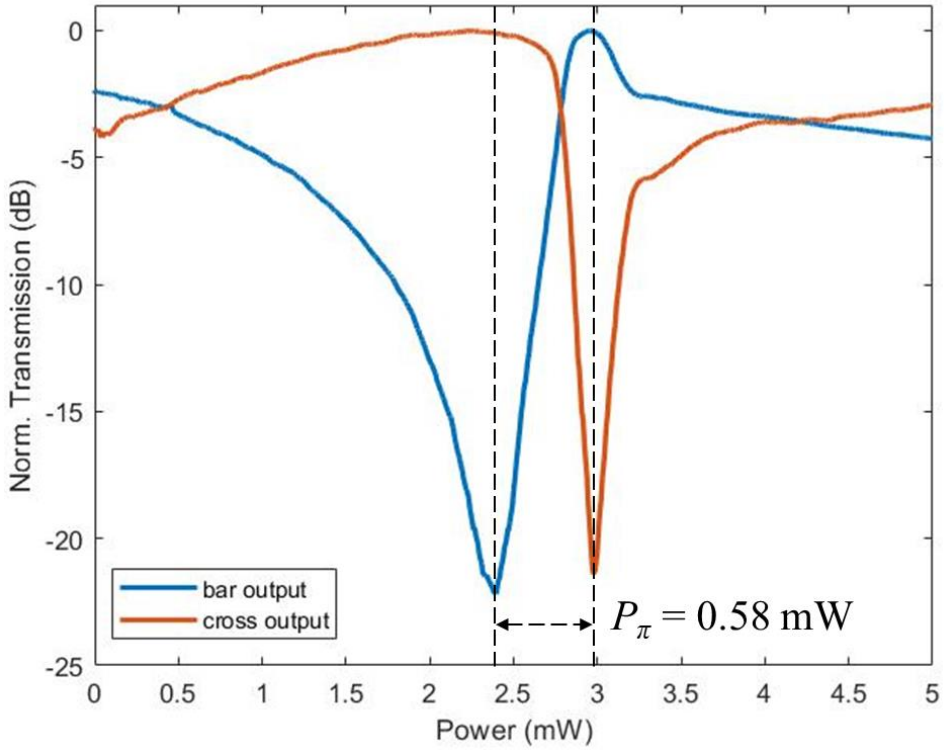

Figure 5.9: The measured optical transmission results as a function of power applied from the 5CB TO switch.

The temporal responses while periodically switched ON/OFF are shown in **Figure 5.10**. The driving signal is square-wave at 5 kHz. The cooling (rise) time constant $\tau_{cooling}$ and heating

(fall) time constant $\tau_{heating}$ measured are 8.4 μs and 11.8 μs, respectively. Same as the results shown in **Figure 5.7**, the 5CB device also has a slower $\tau_{heating}$ due to the nonlinear TO responses mentioned in the last section. The FOM calculated for the 5CB device is 6.8 nW·s.

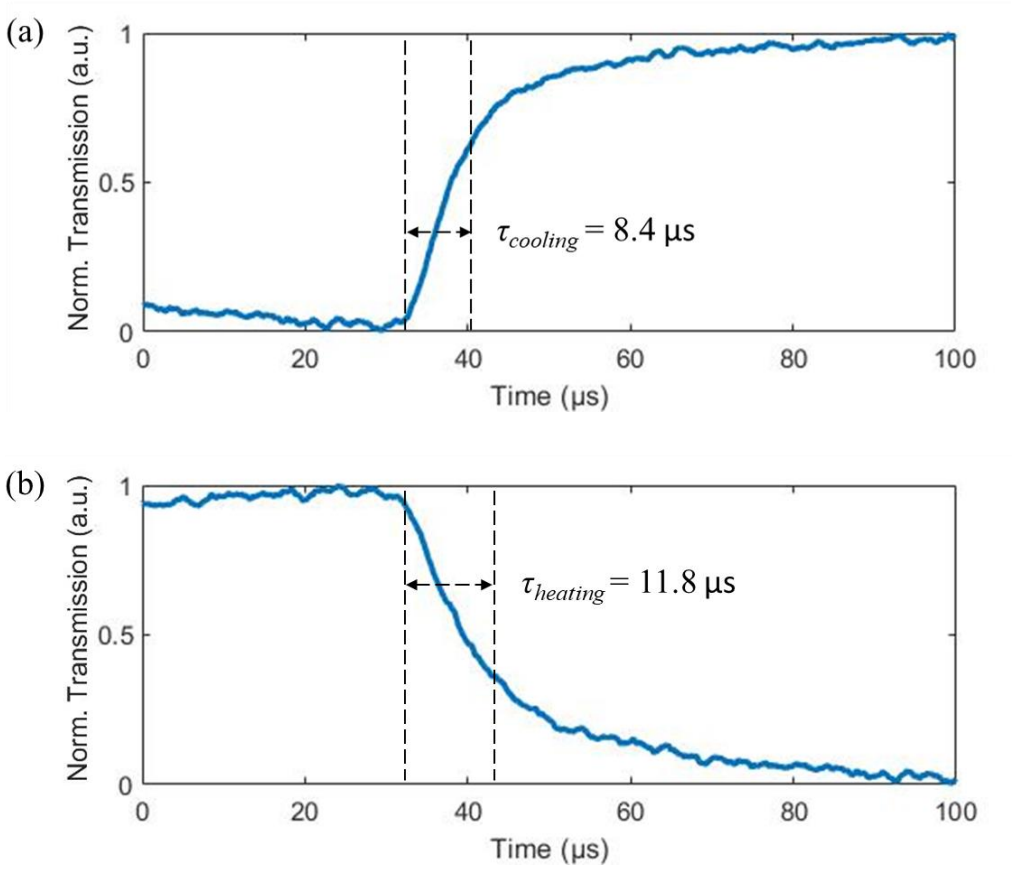

Figure 5.10: Measured temporal responses of the 5CB TO switch for (a) switching ON (cooling) and (b) switching OFF (heating).

5.6 Discussion

Using SWGs to align the NLC in the slot region passively is the core idea for this work. The NLC fills the nano-grooves formed by the SWGs and slot waveguide arms. The shape and aspect ratio of the nano-grooves are critical to realizing proper NLC alignment [113]. Long-

shaped nano-grooves with large aspect ratios are desirable for more uniformly aligned NLC molecules. Due to the sidewall anchoring effect, the NLC aligns parallelly with the long-shaped nano-grooves. However, at both tip regions of the nano-groove array, the NLC orientations are complex. Having a large aspect ratio helps reduce the volume percentage of these tip regions and provides a better overall alignment condition. For low propagation loss, a small grating pitch Λ was required based on **Equation 5.5**. A small silicon filling factor of the SWGs can reserve larger rooms of the nano-grooves for NLC filling and its strong TO effect. However, the smallest silicon filling factor is limited by the fabrication capability in minimum feature size.

Besides the alignment function, the silicon SWGs facilitate heat transfer of the NLC in the slot. Silicon is a good heat conductor (thermal conductivity k_{Si} = 148 W/m·k [111]), whereas NLC materials are not (k_{NLC} ~ 0.2 W/m·k [117]). The thermal energy required to increase the NLC in the slot region is reduced, resulting in a lower heat capacity H and faster response time. Therefore, although the silicon SWGs structure reduces the volume percentage of NLC in the slot, it has the functions of passive alignment and efficient heat transfer.

The demonstrated FOM values are 39.6 nW·s for the E7 device and 6.8 nW·s for the 5CB device. To serve as a benchmark, an optimized pure-SOI MZI TO switch was reported to have an FOM of 50.2 nW·s [113]. It has the same n++ silicon heaters design and a similar waveguide cross-section design. As analyzed in Chapter 2, the MZI configuration has better tuning efficiency (~20%) inherently compared to the directional coupler configuration. An FOM even smaller than 6.8 nW·s can be projected if our proposed technique was utilized in an MZI configuration.

The power consumption and speed of the device can be further optimized by modifying the silicon geometric parameters or using another specially tailored NLC material. The nano-

groove array design and the corresponding NLC alignment effect are worth further systematic studies. Once the correlations are quantitatively determined, the nano-grooves part can also be optimized for better device performance.

5.7 Conclusion

Two silicon TO switches integrated with NLC passively aligned by SWGs were demonstrated. For the E7 device, a P_π of 3.7 mW and a τ of 10.7 μs were measured, corresponding to an FOM of 39.6 nW·s. For the 5CB device, a P_π of 0.58 mW and a τ of 11.8 μs were measured, corresponding to an FOM of 6.8 nW·s. As a comparison, an optimized pure-SOI MZI TO switch with a similar cross-section design was reported to have an FOM of 50.2 nW·s. The proposed technique enhances the TO efficiency and maintains a high speed of the silicon TO switch without electric bias across the nano-slot. The proposed design provides a new solution to achieve low power consumption, high speed, and compact footprint for silicon TO switches.

5.8 Acknowledgement

Chapter 5, in part (Section 5.1-5.4), is a modified reprint of Li-Yuan Chiang, Hao-Chi Liao, Chun-Ta Wang, Steve Pappert, and Paul K.L. Yu, "Enhanced Thermo-Optic Efficiency of Silicon Photonic Switch with Passively Aligned Nematic Liquid Crystals," *Photonics in Switching and Computing*, (PSC, 2021), Tu3A.3 with additional details. The rest of Chapter 5 is currently being prepared for submission for publication of the material. Li-Yuan Chiang, Chun-Ta Wang, Steve Pappert, and Paul K.L. Yu. The dissertation author was the primary investigator and author of these materials. I would like to acknowledge the Office of Naval Research (ONR) (contract N00014-18-I-2027) for the support of this work.

Chapter 6

Conclusion and future work

6.1 Summary of accomplishments in this dissertation

This dissertation demonstrated several high-performance silicon photonic devices based on the silicon-NLC directional coupler configuration for wavelengths near 1550 nm. The slot waveguide directional coupler device platform is the backbone of this dissertation. Unlike the widely used MZI configuration, it does not require additional splitter/combiner pair, routing waveguides, and strip-to-slot mode converters. The advantages of facilitating low-loss and ultra-compact device design with the directional coupler configuration over the MZI configuration were shown with an $L < 400$ μm. The strip-loaded waveguide structure enables a highly confined electric field for EO devices and efficient heat transfer paths for TO devices. NLC materials were integrated into the device platform to break the device performance limitations utilizing the superior material properties of organic NLC materials. The NLC material to be combined with the silicon photonic devices can be flexibly chosen. The ones used in our demonstrations are commercially available for a benchmark in device performance. The NLC material can be tailored for a specific device functionality to optimize the device performance further.

The investigations were conducted in two parallel directions, EO and TO devices. For the EO devices, a series of systematic simulations were completed with Lumerical MODE to study the correlations between the slot waveguide geometry and tuning efficiency. The results have shown that thinner slabs, thicker silicon waveguides, and narrower slot width generally improve

tuning efficiency. Then a Si-NLC EO switch was experimentally demonstrated based on a slot waveguide directional coupler with an overetched region in the slot. The overetched region was formed using RIE dry etch and BOE wet etch steps to ease the NLC reorientation during electrical control. A record low of $V_\pi L$ = 0.0195 V·mm was measured from the EO switch cladded with E7. The ultralow $V_\pi L$ can be projected as a 19.5 μm long device operated with 1 V V_π, pushing the footprint down to an unreachable level for the MZI configuration based on similar techniques.

For the TO devices, we demonstrated a Si-E7 photonic temperature sensor with a temperature sensitivity up to 1.619 nm/°C. The measured temperature sensitivity is one order of magnitude higher than other reported pure SOI photonic temperature sensors. The directional coupler configuration provides a sub-micron 1D spatial resolution for temperature sensing. However, the proposed temperature sensor requires an external electric field to align the NLC in the slot during sensing, which is not ideal for practical applications. We then developed a passive technique to align the NLC in the slot by SWGs and nano-grooves. The passive NLC alignment technique was utilized to demonstrate a power-efficient TO switch. With two n^{++} silicon heaters integrated into the slabs, the P_π measured is 0.58 mW for the 5CB device. The corresponding FOM is 6.8 nW·s, whereas an optimized pure-SOI MZI TO switch with a similar design was reported having an FOM of 50.2 nW·s. The proposed TO switch design paves a new way to achieve low power consumption, high speed, and compact footprint for silicon TO switches.

6.2 Future work

6.2.1 Control of NLC orientation

EO tuning of NLC relies on the molecules' reorientation in response to an external

electric field. The reorientation effect is dependent on the slot width of a slot waveguide. At the silicon sidewalls, there is a boundary anchoring effect hindering the reorientation of NLC molecules. The boundary anchoring can affect a certain distance into the NLC medium dependent on the anchoring strength. The boundary anchoring becomes more significant for a narrow gap. That is one of the reasons why a narrower slot width provides a stronger electric field at fixed applied voltage but not always a better $V_{\pi}L$.

Although the cell gap effect on NLC was reported [108], the studies were conducted with the traditional NLC cell gap sizes at the μm level. For slot waveguide devices, the slot widths are usually in the range of 100-200 nm. Furthermore, a traditional NLC cell consists of two parallel plates. The related studies on cell gap only need to consider 1D confinement. However, in a slot waveguide case, there are fringes from the silicon sidewalls and a solid boundary from the bottom of the slot. The model cannot be simplified to a 1D case due to the comparable dimensions of those factors. A quantitative study has not been reported for the NLC-filled slot waveguide case in the gap size effect.

A systematic study of the size effect of nano-slot on NLC reorientation can be addressed in two aspects. Firstly, slot waveguide devices with different slot widths can be tested to obtain an optimal slot width for EO applications. The optimal slot width may vary with different silicon sidewall thickness, sidewall angle, and geometry of the slot bottom boundary. Secondly, slot waveguide devices with different slot bottom geometry can be tested. The various bottom boundaries are SiO_2 and can be shaped by different etching recipes and steps. The study can help identify the shape and depth effect from the overetched region. Knowing the slot size and geometry effects quantitatively is beneficial for the future development of NLC-filled slot waveguide devices.

The size effect to NLC is also an intriguing topic to the TO switch proposed in Chapter 5. Although not relying on NLC reorientation, the operation principle requires proper NLC alignment through a nano-groove array in the slot. The alignment effect depends on the dimensions and aspect ratio of the nano-grooves. The effect was demonstrated and discussed in [115], but it has not been quantitatively studied. The devices shown in Chapter 5 possess a slot width of 300 nm for an aspect ratio ≥ 3. If the correlations between nano-groove geometry, dimensions, and aspect ratio were quantitatively determined, the device design would be more flexible and easier to optimize.

6.2.2 Spiral TO actuators

TO switches and TO phase shifters share the exact thermal actuation mechanism. The technique proposed in Chapter 5 to enhance TO efficiency is viable to make power-efficient phase shifters as well. As shown in Chapter 2, the modulation efficiency is higher if the actuator is a phase shifter in an MZI switch than a directional coupler switch. This will lead to lower power consumption for TO phase shifters. The following discussion regards an advanced device configuration, which can be incorporated into the two kinds of TO actuators.

As shown in **Figure 5.2**, the n++ heater configuration has two heaters formed at both horizontal sides of the slot waveguide. The thermal energy generated at the heaters is partially transferred to the slot waveguide to realize thermal actuation. The rest of thermal energy is transferred toward other unwanted directions (upward, outward, and downward in this case) and inevitably contributes to excess heat dissipation. Spiral waveguides were developed to reduce the excess heat dissipation to unwanted directions [119-120]. Since spiral waveguides are closely packed, different portions of the spiral waveguides are heated together. The thermally induced

phase shift accumulates and reaches π with a smaller P_π compared to the case of straight TO actuators. With the n++ heater configuration, the TO actuator can be designed as a spiral waveguide and a spiral heater placed between the waveguide sections. The waveguide cross-section views will show the waveguide and heater sections repetitively in the horizontal direction. There will be heated waveguide sections at both sides of each heater section, significantly reducing the excess heater transfer and the resulting P_π. The additional design consideration of using the spiral waveguide configuration is optical crosstalk. Careful design is required to minimize the distance between heater and waveguide sections while maintaining negligible optical crosstalk between waveguides.

6.2.3 System-level demonstrations

This dissertation focuses on device-level developments and demonstrations. After optimizing the performance of individual devices, the next step would be system-level demonstrations. It may include large-scale arrays of the same element and integration with other types of elements. There will be additional design considerations when the development goes to the system-level design. Potential directions of system-level demonstrations are covered in the following discussion for the individual devices proposed from Chapter 3 to Chapter 5.

For the EO switch proposed in Chapter 3, the future work can be switch arrays to demonstrate switch-based optical beam steering [47-51]. Other than the footprint and optical loss discussed in the device-level design, yield and fabrication process control become critical as well in the system-level design. Due to the cascaded fabrics, one defective switch element could result in many malfunctioned channels in switch-based beam steering chips. Fabrication errors and non-uniformity will cause variations in the operating voltages among switch elements.

Calibration of each switch element is required to demonstrate the best switching performance of a switch array.

For the temperature sensor proposed in Chapter 4, it can be integrated as a 1D sensor array for on-chip temperature mapping and monitoring with sub-micron 1D spatial resolution. Although the design in Chapter 4 included metal electrodes that limit the pitch of a 1D sensor array, the metal electrodes can be eliminated by incorporating the passive alignment technique shown in Chapter 5. The device length of each sensor can be adjusted without affecting the sensitivity.

For the TO actuator proposed in Chapter 5, The power-efficient characteristic is desirable for large-scale demonstrations in applications utilizing TO actuators, including but not limited to optical communication [1], photonic FPGA [6], and OPA [41-45]. The compact footprint of directional coupler switches is particularly attractive for photonic FPGA demonstrations with 2D hexagonal mesh structures, as the effect of short device length is squared in cascaded 2D meshes. Besides the power consumption, footprint, loss, yield, and process control, large-scale demonstrations of TO actuators are practical with negligible thermal crosstalk. TO devices need to be placed a distance away from adjacent ones to avoid thermal crosstalk originating from the heat radiation.

References

1. Q. Cheng, M. Bahadori, M. Glick, S. Rumley, and K. Bergman, "Recent advances in optical technologies for data centers: a review," *Optica* **5**, 1354-1370 (2018).

2. C.-P. Hsu, B. Li, B. Solano-Rivas, A. R. Gohil, P. H. Chan, A. D. Moore, and V. Donzella, "A Review and Perspective on Optical Phased Array for Automotive LiDAR," *IEEE Journal of Selected Topics in Quantum Electronics* **27**(1), 1-16 (2021).

3. N. C. Harris, D. Bunandar, M. Pant, G. R. Steinbrecher, J. Mower, M. Prabhu, T. Baehr-Jones, M. Hochberg, and D. Englund, "Large-scale quantum photonic circuits in silicon," *Nanophotonics* **5**(3), 456-468 (2016).

4. B. J. Shastri, A. N. Tait, T. Ferreira de Lima, W. H. P. Pernice, H. Bhaskaran, C. D. Wright, and P. R. Prucnal, "Photonics for artificial intelligence and neuromorphic computing," *Nature Photonics* **15**, 102–114 (2021).

5. E. Luan, H. Shoman, D. M. Ratner, K. C. Cheung, and L. Chrostowski, "Silicon Photonic Biosensors Using Label-Free Detection," *Sensors* **18**(10), 3519 (2018).

6. W. Bogaerts, D. Pérez, J. Capmany, D. A. B. Miller, J. Poon, D. Englund, F. Morichetti, and A. Melloni, "Programmable photonic circuits," *Nature* **586**, 207–216 (2020).

7. G. T. Reed, and A. P. Knights, "*Silicon photonics: an introduction*," John Wiley & Sons (2004).

8. K. Suzuki, G. Cong, K. Tanizawa, S.-H. Kim, K. Ikeda, S. Namiki, and H. Kawashima, "Ultra-high-extinction-ratio 2 × 2 silicon optical switch with variable splitter," *Opt. Express* **23**, 9086-9092 (2015).

9. B. G. Lee and N. Dupuis, "Silicon Photonic Switch Fabrics: Technology and Architecture," *Journal of Lightwave Technology* **37**, 6-20 (2019).

10. J. V. Campenhout, W. M. J. Green, S. Assefa, and Y. A. Vlasov, "Low-power, 2×2 silicon electro-optic switch with 110-nm bandwidth for broadband reconfigurable optical networks," *Opt. Express* **17**, 24020-24029 (2009).

11. A. Densmore, S. Janz, R. Ma, J. H. Schmid, D.-X. Xu, A. Delâge, J. Lapointe, M. Vachon, and P. Cheben, "Compact and low power thermo-optic switch using folded silicon waveguides," *Opt. Express* **17**, 10457-10465 (2009).

12. S. Chung, M. Nakai, and H. Hashemi, "Low-power thermo-optic silicon modulator for large-scale photonic integrated systems," *Opt. Express* **27**, 13430-13459 (2019).

13. G.-D. Kim, H.-S. Lee, C.-H. Park, S.-S. Lee, B. T. Lim, H. K. Bae, and W.-G. Lee, "Silicon

photonic temperature sensor employing a ring resonator manufactured using a standard CMOS process," *Opt. Express* **18**, 22215-22221 (2010).

14. K. V. Shanthi, S. Robinson, "Two-dimensional photonic crystal based sensor for pressure sensing," *Photonic Sens* **4**, 248–253 (2014).

15. S. A. Kolpakov, N. T. Gordon, C. Mou, and K. Zhou, "Toward a New Generation of Photonic Humidity Sensors," *Sensors* **14**(3), 3986-4013 (2014).

16. C. Ranacher, C. Consani, N. Vollert, A. Tortschanoff, M. Bergmeister, T. Grille, and B. Jakoby, "Characterization of Evanescent Field Gas Sensor Structures Based on Silicon Photonics," *IEEE Photonics Journal*, **10**(5), 1-14 (2018).

17. P. Steglich, M. Hulsemann, B. Dietzel, and A. Mai, "Optical biosensors based on silicon-on-insulator ring resonators: A review," *Molecules*, **24**(3), 519 (2019).

18. H. Sakamoto, Y. Minpou, T. Sawai, Y. Enami, S. Suye, "A Novel Optical Biosensing System Using Mach-Zehnder-Type Optical Waveguide for Influenza Virus Detection," *Appl Biochem Biotechnol.* **178**(4), 687-94 (2016).

19. P. J. Collings and M. Hird, "Introduction to Liquid Crystals Chemistry and Physics," *Taylor & Francis: London*, (1997).

20. T. Geelhaar, "Liquid crystals for display applications," *Liquid crystals* **24**(1), 91-98 (1998).

21. V. R. Almeida, Q. Xu, C. A. Barrios, and M. Lipson, "Guiding and confining light in void nanostructure," *Opt. Lett.* **29**, 1209-1211 (2004).

22. F. Dell'Olio and V. M. N. Passaro, "Optical sensing by optimized silicon slot waveguides," *Opt. Express* **15**, 4977-4993 (2007).

23. A. Martínez, J. Blasco, P. Sanchis, J. V. Galán, J. García-Rupérez, E. Jordana, P. Gautier, Y. Lebour, S. Hernández, R. Spano, R. Guider, N. Daldosso, B. Garrido, J. M. Fedeli, L. Pavesi, and J. Martí, "Ultrafast Ultrafast All-Optical Switching in a Silicon-Nanocrystal-Based Silicon Slot Waveguide at Telecom Wavelengths," *Nano Letters* **10**(4), 1506-1511 (2010).

24. T. Claes, J. Girones Molera, K. De Vos, E. Schacht, R. Baets and P. Bienstman, "Label-Free Biosensing With a Slot-Waveguide-Based Ring Resonator in Silicon on Insulator," *IEEE Photonics Journal* **1**(3), 197-204 (2009).

25. I. Goncharenko and M. Marciniak, "Optical temperature sensor on the base of slot waveguide with LC filling," *2012 14th International Conference on Transparent Optical Networks (ICTON)*, 1-5 (2012).

26. R. Ding, T. Baehr-Jones, Y. Liu, R. Bojko, J. Witzens, S. Huang, J. Luo, S. Benight, P. Sullivan, J-M Fedeli, M. Fournier, L. Dalton, A. Jen, and M. Hochberg, "Demonstration of a low $V_{\pi}L$ modulator with GHz bandwidth based on electro-optic polymer-clad silicon slot

waveguides," *Opt. Express* **18**, 15618-15623 (2010).

27. R. Ding, T. Baehr-Jones, W.-J. Kim, X. Xiong, R. Bojko, J.-M. Fedeli, M. Fournier, and M. Hochberg, "Low-loss strip-loaded slot waveguides in Silicon-on-Insulator," *Opt. Express* **18**, 25061-25067 (2010).

28. R. Palmer, L. Alloatti, D. Korn, P. C. Schindler, M. Baier, J. Bolten, T. Wahlbrink, M. Waldow, R. Dinu, W. Freude, C. Koos, and J. Leuthold, "Low Power Mach–Zehnder Modulator in Silicon-Organic Hybrid Technology," *IEEE Photonics Technol. Lett.* **25(**13), 1226-1229 (2013).

29. Q. Deng, L. Liu, X. Li, and Z. Zhou, "Strip-slot waveguide mode converter based on symmetric multimode interference," *Opt. Lett.* **39**, 5665-5668 (2014).

30. G. B. Cao, F. Gao, J. Jiang, and F. Zhang, "Directional couplers realized on silicon-on-insulator," *IEEE Photonics Technol. Lett.* **17**(8), 1671–1673 (2005).

31. J. Xing, K. Xiong, H. Xu, Z. Li, X. Xiao, J. Yu, and Y. Yu, "Silicon-on-insulator-based adiabatic splitter with simultaneous tapering of velocity and coupling," *Opt. Lett.* **38**(13), 2221–2223 (2013).

32. L. B. Soldano and E. C. M. Pennings, "Optical multi-mode interference devices based on self-imaging: principles and applications," *Journal of Lightwave Technology* **13**(4), 615–627 (1995).

33. P. Dumais, Y. Wei, M. Li, F. Zhao, X. Tu, J. Jiang, D. Celo, D. J. Goodwill, H. Fu, D. Geng, and E. Bernier, "2x2 multimode interference coupler with low loss using 248 nm photolithography," *Optical Fiber Communication Conference*, (OFC, 2016), W2A.19.

34. C. A. Barrios, V. R. Almeida, R. Panepucci, and M. Lipson, "Electrooptic modulation of silicon-on-insulator submicrometer-size waveguide devices," *Journal of Lightwave Technology* **21**(10), 2330–2332 (2003).

35. S. Manipatruni, Q. Xu, B. Schmidt, J. Shakya, and M. Lipson, "High speed carrier injection 18 Gb/s silicon micro-ring electro-optic modulator," *Lasers Electro-Opt. Soc.* **20**, 537–538 (2007).

36. L.-Y. Chiang, C.-T. Wang, T.-S. Lin, S. Pappert, and P. Yu, "Highly sensitive silicon photonic temperature sensor based on liquid crystal filled slot waveguide directional coupler," *Opt. Express* **28**, 29345-29356 (2020).

37. J. Li and S.-T. Wu, "Infrared refractive indices of liquid crystals," *Journal of Applied Physics* **97**, 073501 (2005).

38. L.-Y. Chiang, C.-T. Wang, S. Pappert, and P. K.L. Yu, "Efficient silicon photonic waveguide switches for chip-scale beam steering applications," *5th IEEE Electron Devices Technology & Manufacturing Conference*, (EDTM, 2021), WE2P2-3.

39. Y. Choi, H. Yokoyama, and J. S. Gwag, "Determination of surface nematic liquid crystal anchoring strength using nano-scale surface grooves," *Opt. Express* **21**, 12135-12144 (2013).

40. Y. Xing, T. Ako, J. P. George, D. Korn, H. Yu, P. Verheyen, M. Pantouvaki, G. Lepage, P. Absil, A. Ruocco, C. Koos, J. Leuthold, Kristiaan Neyts, J. Beeckman, and W. Bogaerts, "Digitally Controlled Phase Shifter Using an SOI Slot Waveguide With Liquid Crystal Infiltration," *IEEE Photonics Technol. Lett.* **27**(12), 1269-1272 (2015).

41. J. K. Doylend, M. J. R. Heck, J. T. Bovington, J. D. Peters, L. A. Coldren, and J. E. Bowers, "Two-dimensional free-space beam steering with an optical phased array on silicon-on-insulator," *Opt. Express* **19**, 21595-21604 (2011).

42. J. Sun, E. Timurdogan, A. Yaacobi, E. S. Hosseini, and M. R. Watts, "Large-scale nanophotonic phased array," *Nature* **493**, 195-199 (2013).

43. D. Kwong, A. Hosseini, J. Covey, Y. Zhang, X. Xu, H. Subbaraman, and R. T. Chen, "On-chip silicon optical phased array for two-dimensional beam steering," *Opt. Lett.* **39**, 941-944 (2014).

44. Y. Zhang, Y.-C. Ling, K. Zhang, C. Gentry, D. Sadighi, G. Whaley, J. Colosimo, P. Suni, and S. J. B. Yoo, "Sub-wavelength-pitch silicon-photonic optical phased array for large field-of-regard coherent optical beam steering," *Opt. Express* **27**, 1929-1940 (2019).

45. C.-P. Hsu, B. Li, B. Solano-Rivas, A. R. Gohil, P. H. Chan, A. D. Moore, and V. Donzella, "A review and perspective on optical phased array for automotive LiDAR," *IEEE J. Sel. Top. Quantum Electron.* **27**(1), 1-16 (2021).

46. R. Halterman and M. Bruch, "Velodyne HDL-64E lidar for unmanned surface vehicle obstacle detection," *Proc. SPIE* **7692**, 76920D (2010).

47. J. J. López, S. A. Skirlo, D. Kharas, J. Sloan, J. Herd, P. Juodawlkis, M. Soljačić, and C. Sorace-Agaskar, "Planar-lens enabled beam steering for chip-scale LIDAR," *Conference on Lasers and Electro-Optics*, (CLEO, 2018), SM3I.1.

48. D. Inoue, T. Ichikawa, A. Kawasaki, and T. Yamashita, "Demonstration of a new optical scanner using silicon photonics integrated circuit," *Opt. Express* **27**, 2499-2508 (2019).

49. C. Li, X. Cao, K. Wu, X. Li, and J. Chen, "Lens-based integrated 2D beam-steering device with defocusing approach and broadband pulse operation for Lidar application," *Opt. Express* **27**, 32970-32983 (2019).

50. H. Ito, Y. Kusunoki, J. Maeda, D. Akiyama, N. Kodama, H. Abe, R. Tetsuya, and T. Baba, "Wide beam steering by slow-light waveguide gratings and a prism lens," *Optica* **7**, 47-52 (2020).

51. S. J. Spector, "Review of lens-assisted beam steering methods," *J. of Optical Microsystems*

2(1), 011003 (2022).

52. X. Tu, C. Song, T. Huang, Z. Chen, and H. Fu, "State of the art and perspectives on silicon photonic switches," *Micromachines* **10**(1), 51 (2019).

53. M. Li, L. Wang, X. Li, X. Xiao, and S. Yu, "Silicon intensity Mach–Zehnder modulator for single lane 100 Gb/s applications," *Photon. Res.* **6**, 109-116 (2018).

54. T. Baehr-Jones, B. Penkov, J. Huang, P. Sullivan, J. Davies, J. Takayesu, J. Luo, T.-D. Kim, L. Dalton, A. Jen, M. Hochberg, and A. Scherer, "Nonlinear polymer-clad silicon slot waveguide modulator with a half wave voltage of 0.25V," *Appl. Phys. Lett.* **92**, 163303 (2008).

55. C.-Y. Lin, X. Wang, S. Chakravarty, B. S. Lee, W. Lai, J. Luo, A. K.-Y. Jen, and R. T. Chen, "Electro-optic polymer infiltrated silicon photonic crystal slot waveguide modulator with 23 dB slow light enhancement," *Appl. Phys. Lett.* **97**, 093304 (2010).

56. R. Ding, T. Baehr-Jones, Y. Liu, R. Bojko, J. Witzens, S. Huang, J. Luo, S. Benight, P. Sullivan, J-M Fedeli, M. Fournier, L. Dalton, A. Jen, and M. Hochberg, "Demonstration of a low VπL modulator with GHz bandwidth based on electro-optic polymer-clad silicon slot waveguides," *Opt. Express* **18(**15), 15618–15623 (2010).

57. C. Kieninger, C. Füllner, H. Zwickel, Y. Kutuvantavida, J. N. Kemal, C. Eschenbaum, D. L. Elder, L. R. Dalton, W. Freude, S. Randel, and C. Koos, "Silicon-organic hybrid (SOH) Mach-Zehnder modulators for 100 GBd PAM4 signaling with sub-1 dB phase-shifter loss," *Opt. Express* **28**, 24693–24707 (2020).

58. J. Pfeifle, L. Alloatti, W. Freude, J. Leuthold, and C. Koos, "Silicon-organic hybrid phase shifter based on a slot waveguide with a liquid-crystal cladding," *Opt. Express* **20**, 15359-15376 (2012).

59. J. Ptasinski, S. W. Kim, L. Pang, I.-C. Khoo, and Y. Fainman, "Optical tuning of silicon photonic structures with nematic liquid crystal claddings," *Opt. Lett.* **38**(12), 2008–2010 (2013).

60. C.-T. Wang, Y.-C. Li, J.-H. Yu, C. Y. Wang, C.-W. Tseng, H.-C. Jau, Y.-J. Chen, and T.-H. Lin, "Electrically tunable high Q-factor micro-ring resonator based on blue phase liquid crystal cladding," *Opt. Express* **22**, 17776-17781 (2014).

61. W. Heni, C. Haffner, D. L. Elder, A. F. Tillack, Y. Fedoryshyn, R. Cottier, Y. Salamin, C. Hoessbacher, U. Koch, B. Cheng, B. Robinson, L. R. Dalton, and J. Leuthold, "Nonlinearities of organic electro-optic materials in nanoscale slots and implications for the optimum modulator design," *Opt. Express* **25**, 2627-2653 (2017).

62. Y. Atsumi, T. Miyazaki, N. Miura, M. Mori, and Y. Sakakibara, "Compact and low-loss liquid crystal loaded Mach-Zehnder optical switch based on Si wire waveguide," *IEICE Electron. Express* **14**(6), 20170110 (2017).

63. L.-Y. Chiang, C.-T. Wang, S. Pappert, and P. K.L. Yu, "Ultralow-$V_{\pi}L$ Silicon Electro-Optic Directional Coupler Switch With a Liquid Crystal Cladding," *IEEE Photonics Technol. Lett.* **33**(15), 796-799 (2021).

64. R. Asquini, C. Chiccoli, A. d'Alessandro, P. Pasini, and C. Zannoni, "Monte Carlo study of slot-waveguide liquid crystal phase shifters," *Mol. Cryst. Liq. Cryst*. **683**, 46-55 (2019).

65. S. H. Perlmutter, D. Doroski, and G. Moddel, "Degradation of liquid crystal device performance due to selective adsorption of ions," *Appl. Phys. Lett.* **69**, 1182 (1996).

66. D. L. Cheung and F. Schmid, "Monte Carlo simulations of liquid crystals near rough walls," *J. Chem. Phys.* **122**(7), 074902 (2005).

67. M. Jiao, Z. Ge, Q. Song, and S.-T. Wu, "Alignment layer effects on thin liquid crystal cells," *Appl. Phys. Lett.* **92(**6), 061102 (2008).

68. D. J. Thomson, Y. Hu, G. T. Reed, and J. Fedeli, "Low loss MMI couplers for high performance MZI modulators," *IEEE Photon. Technol. Lett.* **22**(20), 1485-1487 (2010).

69. R. Palmer, L. Alloatti, D. Korn, W. Heni, P. C. Schindler, J. Bolten, M. Karl, M. Waldow, T. Wahlbrink, W. Freude, C. Koos, and J. Leuthold, "Low-loss silicon strip-to-slot mode converters," *IEEE Photon. J.* **5**(1), 2200409-2200409 (2013).

70. S. Gauza, C.-H. Wen, B. Wu, S.-T. Wu, A. Spadlo, and R. Dabrowski, "High figure-of-merit nematic mixtures based on totally unsaturated isothiocyanate liquid crystals," *Liq. Cryst.* **33**, 705-710 (2007).

71. M. Raicopol, C. Dascalu, R. Atasiei, and A.-L. Alexe-Ionescu, "Electro-optic effect in nematic liquid crystals aligned with conductive polymer," *Proc. SPIE 7469, ROMOPTO 2009: Ninth Conference on Optics: Micro- to Nanophotonics II*, 74690K (2010).

72. W. Lee, C.-Y. Wang, and Y.-C. Shih, "Effects of carbon nanosolids on the electro-optical properties of a twisted nematic liquid-crystal host," *Appl. Phys. Lett.* **85**(4), 513-515 (2004).

73. D. N. Chausov, A. D. Kurilov, R. N. Kucherov, A. V. Simakin, and S. V. Gudkov, "Electro-optical performance of nematic liquid crystals doped with gold nanoparticles," *J. Phys. Condens. Matter* **32**, 395102 (2020).

74. J. Kumar, R. K. Gupta, S. Kumar, and V. Manjuladevi, "Electro-Optic and Dielectric Studies on Quantum Dot Doped Nematic Liquid Crystal," *Macromolecular Symposia* **357**, 47–51 (2015).

75. H.-R. Kim, E. Jang, and S.-D. Lee, "Electrooptic temperature sensor based on a Fabry–Pérot resonator with a liquid crystal film," *IEEE Photonics Technol. Lett.* **18**(8), 905–907 (2006).

76. S. J. Mihailov, "Fiber Bragg grating sensors for harsh environments," *Sensors* **12**(2), 1898-

918 (2012).

77. T. Muñoz-Hernandez, E. Reyes-Vera, and P. Torres, "Temperature Sensor Based on Whispering Gallery Modes of Metal-Filled Side-Hole Photonic Crystal Fiber Resonators," *IEEE Sens. J.* **20**(16), 9170-9178 (2020).

78. R. Wang, Q. Wu, X. Jiang, T. Fan, J. Guo, C. Wang, F. Zhang, Y. Gao, M. Zhang, Z. Luo, and H. Zhang, "A few-layer InSe-based sensitivity-enhanced photothermal fiber sensor," *J. Mater. Chem. C* **8**(1), 132-138 (2020).

79. E.Reyes-Vera, C. M. B. Cordeiro, and P. Torres, "Highly sensitive temperature sensor using a Sagnac loop interferometer based on a side-hole photonic crystal fiber filled with metal," *Appl. Opt.* **56**, 156-162 (2017).

80. Y. Li, G.-F. Yan, and S. He, "Thin-Core Fiber Sandwiched Photonic Crystal Fiber Modal Interferometer for Temperature and Refractive Index Sensing," *IEEE Sens. J.* **18**(16), 6627-6632 (2018).

81. G. Chesini, J. H. Osório, V. A. Serrão, M. A. R. Franco, and C. M. B. Cordeiro, "Metal-Filled Embedded-Core Capillary Fibers as Highly Sensitive Temperature Sensors," *IEEE Sens. Lett.* **2**(2), 1-4 (2018).

82. I. S. Amiri, P. Yupapin, M. M. Ariannejad, and S. Daud, "High sensitive temperature sensor silicon-based microring resonator using the broadband input spectrum," *Results Phys.* **9**, 1578–1584 (2018).

83. D. Niu, X. Wang, S. Sun, M. Jiang, Q. Xu, F. Wang, Y. Wu, and D. Zhang, "Polymer/silica hybrid waveguide temperature sensor based on asymmetric Mach–Zehnder interferometer," *J. Opt.* **20**(4), 045803 (2018).

84. R. Dwivedi and A. Kumar, "Ultrahigh-sensitive temperature sensor based on modal interference in a metal-under-clad ridge waveguide with a polymer upper cladding," *Appl. Opt.* **56**(16), 4685–4689 (2017).

85. D. Niu, L. Wang, Q. Xu, M. Jiang, X. Wang, X. Sun, F. Wang, and D. Zhang, "Ultra-sensitive polymeric waveguide temperature sensor based on asymmetric Mach–Zehnder interferometer," *Appl. Opt.* **58**(5), 1276–1280 (2019).

86. Y. Zhang, J. Zou, and J.-J. He, "Temperature sensor with enhanced sensitivity based on silicon Mach-Zehnder interferometer with waveguide group index engineering," *Opt. Express* **26**, 26057-26064 (2018).

87. J.-M. Lee, "Ultrahigh temperature-sensitive silicon MZI with titania cladding," *Front. Mater.* **2**, 36 (2015).

88. X. Guan, X. Wang, and L. H. Frandsen, "Optical temperature sensor with enhanced sensitivity by employing hybrid waveguides in a silicon Mach-Zehnder interferometer," *Opt.*

Express **24**, 16349-16356 (2016).

89. A. Irace and G. Breglio, "All-silicon optical temperature sensor based on Multi-Mode Interference," *Opt. Express* **11**(22), 2807–2812 (2003).

90. H.-T. Kim and M. Yu, "Cascaded ring resonator-based temperature sensor with simultaneously enhanced sensitivity and range," *Opt. Express* **24**(9), 9501–9510 (2016).

91. H. Xu, M. Hafezi, J. Fan, J. M. Taylor, G. F. Strouse, and Z. Ahmed, "Ultra-sensitive chip-based photonic temperature sensor using ring resonator structures," *Opt. Express* **22**(3), 3098–3104 (2014).

92. N. N. Klimov, S. Mittal, M. Berger, and Z. Ahmed, "On-chip silicon waveguide Bragg grating photonic temperature sensor," *Opt. Lett.* **40**(17), 3934–3936 (2015).

93. H. Yan, X. Xiao, J. Zang, X. Xia, Y. Chen, and Y. Huang, "High-sensitivity temperature sensor by coupling two-dimensional photonic crystal waveguide with dual microcavities," *Opt. Eng.* **57**(10), 1 (2018).

94. Y. Zhang, P. Liu, S. Zhang, W. Liu, J. Chen, and Y. Shi, "High sensitivity temperature sensor based on cascaded silicon photonic crystal nanobeam cavities," *Opt. Express* **24**(20), 23037–23043 (2016).

95. R. Dekker, N. Usechak, M. Forst, and A. Driessen, "Ultrafast nonlinear all-optical processes in silicon-on-insulator waveguides," *J. Phys. D: Appl. Phys.* **40**(14), R249–R271 (2007).

96. I. A. Goncharenko, V. Kireenko, and M. Marciniak, "Optimizing the structure of optical temperature sensors on the base of slot and double-slot ring waveguides with liquid crystal filling," *Opt. Eng.* **53**(7), 071802 (2013).

97. C.-T. Wang, C.-Y. Wang, J.-H. Yu, I.-T. Kuo, C.-W. Tseng, H.-C. Jau, Y.-J. Chen, and T.-H. Lin, "Highly sensitive optical temperature sensor based on a SiN micro-ring resonator with liquid crystal cladding," *Opt. Express* **24**(2), 1002–1007 (2016).

98. V. M. N. Passaro, F. Dell'Olio, B. Casamassima, and F. De Leonardis, "Guided-Wave Optical Biosensors," *Sensors* **7**(4), 508–536 (2007).

99. I.-C. Khoo and S.-T. Wu, Optics and Nonlinear Optics of Liquid Crystals (World Scientific, 1993).

100. J. Li, S. Gauzia, and S.-T. Wu, "High temperature-gradient refractive index liquid crystals," *Opt. Express* **12**(9), 2002–2010 (2004).

101. H. Desmet, K. Neyts, and R. Baets, "Liquid crystal orientation on patterns etched in Silicon on Insulator," *Integrated Optics, Silicon Photonics, and Photonic Integrated Circuits*, Society of Photo-Optical Instrumentation Engineers (SPIE) Conference Series (61831Z), (2006).

102. M. Uenuma and T. Motooka, "Temperature-independent silicon waveguide optical filter," *Opt. Lett.* **34**(5), 599–601 (2009).

103. Y. Kim, B. Senyuk, and O. Lavrentovich, "Molecular reorientation of a nematic liquid crystal by thermal expansion," *Nat. Commun.* **3**(1), 1133 (2012).

104. K. Suzuki, R. Konoike, J. Hasegawa, S. Suda, H. Matsuura, K. Ikeda, S. Namiki, and H. Kawashima, "Low-insertion-loss and power-efficient 32 × 32 silicon photonics switch with extremely high-Δ silica PLC connector," *J. Lightwave Technol.* **37**, 116–122 (2019).

105. N. Alshamrani, A. Grieco, A. Friedman, K. A. Johnson, M.-S. Kim, F. Floris, P. O'brien, and Y. Fainman, "A Non-Mechanical Multi-Wavelength Integrated Photonic Beam Steering System," *J. Lightwave Technol.* **39**, 4201-4208 (2021).

106. D. Pérez, I. Gasulla, and J. Capmany, "Field-programmable photonic arrays," *Opt. Express* **26**, 27265-27278 (2018).

107. Q. Fang, J. F. Song, T.-Y. Liow, H. Cai, M. B. Yu, G. Q. Lo, and D.-L. Kwong "Ultralow Power Silicon Photonics Thermo-Optic Switch With Suspended Phase Arms," *IEEE Photon. Technol. Lett.* **23**(8), 525-527 (2011).

108. L.-Y. Chiang, H.-C. Liao, C.-T. Wang, S. Pappert, and P. K.L. Yu, " Enhanced Thermo-Optic Efficiency of Silicon Photonic Switch with Passively Aligned Nematic Liquid Crystals," *Photonics in Switching and Computing*, (PSC, 2021), Tu3A.3.

109. P. J. Bock, P. Cheben, J. H. Schmid, J. Lapointe, A. Delâge, S. Janz, G. C. Aers, D.-X. Xu, A. Densmore, and T. J. Hall, "Subwavelength grating periodic structures in silicon-on-insulator: a new type of microphotonic waveguide," *Opt. Express* **18**, 20251-20262 (2010).

110. R. Halir, P. J. Bock, P. Cheben, A. Ortega-Moñux, C. Alonso-Ramos, J. H. Schmid, J. Lapointe, D.-X. Xu, J. G. Wangüemert-Pérez, Í. Molina-Fernández, and S. Janz, "Waveguide sub-wavelength structures: a review of principles and applications," *Laser Photonics Rev.* **9**, 25–49 (2015).

111. P. Cheben, R. Halir, J. H. Schmid, H. A. Atwater, and D. R. Smith, "Subwavelength integrated photonics," *Nature* **560**, 565–572 (2018).

112. Y. Atsumi, K. Watabe, N. Uda, N. Miura, and Y. Sakakibara, "Initial alignment control technique using on-chip groove arrays for liquid crystal hybrid silicon optical phase shifters," *Opt. Express* **27**, 8756-8767 (2019).

113. M. Jacques, A. Samani, E. El-Fiky, D. Patel, Z. Xing, and D. V. Plant, "Optimization of thermo-optic phase-shifter design and mitigation of thermal crosstalk on the SOI platform," *Opt. Express* **27**, 10456-10471 (2019).

114. M. R. Watts, J. Sun, C. DeRose, D. C. Trotter, R. W. Young, and G. N. Nielson,

"Adiabatic thermo-optic Mach-Zehnder switch," *Opt. Lett.* **38**(5), 733–735 (2013).

115. H. Desmet, K. Neyts, and R. Baets, "Liquid crystal orientation on patterns etched in Silicon on Insulator," *SPIE Proceedings* **6183**, 455-462 (2006).

116. V. Tkachenko, A. Marino, and G. Abbate, "Study of Nematic Liquid Crystals by Spectroscopic Ellipsometry," *Molecular Crystals and Liquid Crystals* **527**, 80-91 (2010).

117. G. Ahlers, D. S. Cannell, L. I. Berge, and S. Sakurai, "Thermal conductivity of the nematic liquid crystal 4-n-pentyl-4'-cyanobiphenyl," *Physical Review E* **49**(1), 545 (1994).

118. X. Nie, R. Lu, H. Xianyu, T. X. Wu, and S.-T. Wu, "Anchoring energy and cell gap effects on liquid crystal response time," *J. Appl. Phys.* **101**, 103110 (2007).

119. A. Densmore, S. Janz, R. Ma, J. H. Schmid, D.-X. Xu, A. Delâge, J. Lapointe, M. Vachon, and P. Cheben, "Compact and low power thermo-optic switch using folded silicon waveguides," *Opt. Express* **17**, 10457-10465 (2009).

120. H. Qiu, Y. Liu, C. Luan, D. Kong, X. Guan, Y. Ding, and H. Hu, "Energy-efficient thermo-optic silicon phase shifter with well-balanced overall performance," *Opt. Lett.* **45**, 4806-4809 (2020).